Structural, morphological, optical, and electrical studies of Tb-doped ZnO micropods elaborated by chemical bath deposition on a p-Si substrate

Nouf Ahmed Althumairi, Irshad Baig, Tarek Said Kayed, Abdelkarim Mekki, Alain Lusson, Vincent Sallet, Abdul Majid, Sultan Akhtar, Afif Fouzri

Structural, morphological, optical and electrical studies of Tb-doped ZnO micropods elaborated by Chemical Bath Deposition on a p-Si substrate

Nouf Ahmed Althumairi[1,2,3], Irshad Baig[2], Tarek Said Kayed[4], Abdelkarim Mekki[5,6], Alain Lusson[7], Vincent Sallet[7], Abdul MAJID[8], Sultan Akhtar[9], Afif Fouzri[1,2,*]

[1]Department of physics, College of Science, Imam Abdulrahman Bin Faisal University, P.O. Box 1982, Dammam 31441, Saudi Arabia.

[2]Basic & Applied Scientific Research Center, Imam Abdulrahman Bin Faisal University, P.O. Box 1982, Dammam 31441, Saudi Arabia.

[3]Department of Biology, College of Education, Majmaah University, P.O. Box 66, Almajmaah 11952, Saudi Arabia.

[4]Department of Basic Engineering Sciences, College of Engineering, Imam Abdulrahman Bin Faisal University, P.O. Box 1982, Dammam 31441, Saudi Arabia.

[5]Department of Physics, King Fahd University of Petroleum & Minerals, Dhahran 31261, Saudi Arabia.

[6]Interdisciplinary Research Center for Advanced Materials, King Fahd University of Petroleum & Minerals, Dhahran 31261, Saudi Arabia.

[7]Groupe d'Etude de la Matière Condensée (GEMAC), CNRS, Université de Versailles-St Quentin en Yvelines, Université Paris-Saclay, 45 Avenue des Etats-Unis, 78035 Versailles, France.

[8]Department of Physics, College of Science, Zulfi 11932, Majmaah University.

[9]Department of Biophysics, Institute for Research and Medical Consultations (IRMC), Imam Abdulrahman Bin Faisal University, P.O. Box 1982, Dammam 31441, Saudi Arabia.

* Corresponding author (email: Anfouzri@iau.edu.sa)

Abstract:

Terbium-doped zinc oxide microstructures with a hexagonal wurtzite structure were synthesized by a chemical bath deposition (CBD) method on *p*-type (100) silicon. The effects of the amount of Tb incorporated and heat treatment on the physical properties were explored. X-ray photoelectron spectroscopy (XPS) confirme the simultaneous insertion of Tb^{3+} and Tb^{4+} into the ZnO matrix. An increase in the Tb concentration up to 4.21% with annealing temperature is shown by energy dispersive X-ray (EDX) measurements. Scanning electron microscopy (SEM) images show the formation of micropod ZnO with a perfectly smooth hexagonal sidewall shape. This structure of doped ZnO remained stable, although distortion of the distance and tetrahedral bonds was confirmed by XRD analysis. The luminescence spectra of the doped micropods did not show the Tb ion emission lines, proving that no energy transfer from the host to the rare earth ions occurred. However, the visible band emission was deformed, and the International Commission on Illumination (CIE) color emission shifted to green as the concentration of Tb increased. Near white-light emission was observed for Tb-doped ZnO micropods with concentrations higher than 1.4% and annealed at 300° C. The color emission of the Tb-doped ZnO micropods can be tuned by varying the concentrations of Tb in the ZnO host and/or the annealing temperature, which is an interesting aspect for solid-state lighting applications. The dependence of electrical parameters on dopant concentration and annealing temperature was explored by current-voltage (*I-V*) measurements, which showed a small change in barrier height with increasing dopant concentration.

1 Introduction

Many studies have been devoted to the development of electroluminescent materials compatible with silicon technology. Among these materials are thin films or micro/nanostructures of semiconductors or transparent conductive oxides doped with rare earth ions (RE) [1]. It is a known rare earth (RE^{3+}) emitted in the visible-IR spectral region, resulting in stable and multiple sharp bands at a single excitation. A judicious choice of these, embedded in an appropriate transparent and conductive matrix, makes it possible to control the properties of light emission under electrical excitation. The choice of ZnO as the host matrix has several advantages. It is a II-VI *n*-type semiconductor with a wide band gap 3.37 eV and a large exciton binding energy (60 meV) [2] at room temperature higher than the thermal energy (25 meV). It has high thermal and chemical stability and is inexpensive, as it is environmentally friendly. It can grow in various dimensions and shapes, such as micro/nanoparticles, rods, wires, and tubes [3,4]. Moreover, ZnO luminescence in the UV, blue, and green domains allows it to be a good candidate for the realization of LEDs [1,5]. However, without doping, ZnO matrix emission and chromaticity are weak in the visible region which is insufficient for use in solid-state lighting. This broad emission is due to the different king of defect [6,7], as oxygen vacancies (Vo), oxygen interstitials (O_i), zinc vacancies (V_{Zn}), zinc interstitials (Zn_i)… Their relative concentration influence significantly the intensity of visible emission [3,6,7], thereby making it possible to adjust the emission color [8]. Therefore, doping ZnO with rare-earth elements makes it possible to obtain the luminescence of these elements added to that of the matrix. By combining the conductive aspect of ZnO and the luminescence of the rare earth, we can obtain an ideal material for a controllable emission electroluminescent device. Several reports in the literature have investigated light-emitting ZnO doped and co-

doped with different RE ions such as europium, terbium, and cesium [7]. Indeed, RE can absorb the UV-blue emission of ZnO and emit in the visible or infrared range. Several energy transfers from the ZnO host to RE ion models have been proposed [8-10]. In addition, the optical properties of RE-doped ZnO also depend on the dopant concentration, synthesis process, heat treatment, and morphology of the ZnO mico/nano-crystal host. In fact, the 4f core levels ~~for~~ of the RE ions ~~is~~ are very sensitive to the crystal field energy and spin-orbit coupling. The luminescence efficiency of RE ions in ZnO can be significantly influenced by the location of the ion in the host lattice structure, as the RE ion can be placed on an interstitial site (RE_i) and/or it replaces the Zn^{2+} ion. In addition, the large difference in the ionic radius and charge state of the RE and Zn^{2+} ions limits the RE ion incorporation into the ZnO matrix and causes a different distortion of the tetrahedral bonding, inducing a different king of defects. All these factors affect the efficiency of energy transfer from the ZnO host to RE ions, and hence the emission luminescence of the material.

To determinate the possibility of obtaining white-light-emitting diodes by co-doping ZnO micropods with Eu and Tb, and after a recent detailed study [11] of these ZnO microstructures doped with Eu, a similar approach was conducted in this work to explore the effect of heat treatment and Tb concentration on the physical properties of samples prepared using the same procedure. The photometric characteristics, color emission and color-correlated temperature (CCT), was determined based on the CIE chromaticity coordinates.

2 Experimental procedure

2.1 Samples preparation

In our work, the growth of pure and terbium-doped ZnO microstructures on a substrate was performed using the chemical bath deposition (CBD) method. ~~Bore-~~

~~doped~~ Boron-doped *p*-type (100) silicon substrates with a resistivity of 1-10 Ω cm and a thickness of 525 μm were used. The sample preparation procedure was similar to that described in detail in our recently published study [11]. Where a 0.05M zinc acetate dihydrate ($Zn(CH_3CO_2).2H_2O$) (Chem-Impex, 99.18%) was dissolved in 250 ml of deionized water (18 MΩ cm) to prepare the solution. Subsequently, 1 ml of ammonium hydroxide (NH_4OH) (Sigma-Aldrich) was added dropwise to the solution and stirred at room temperature. The synthesis of Tb-doped ZnO was performed by added different amounts of terbium III nitrate pentahydrate ($Tb(NO_3)_3.5H_2O$) (Alfa Aesar, 99.9%) to the zinc acetate precursor in order to get different Tb concentrations. 5%, 10%, 15%, 20%, and 25% weight ratios (wt %) of Tb/Zn were prepared and annealed in an oven for 2 h respectively at T_a=300, 500, and 700 ° C.

2.1 Samples Characterization

The chemical composition and morphology of the prepared samples were determined using a VEGA 3 TESCAN scanning electron microscope (SEM) coupled with an energy dispersive X-ray spectrometer (EDX). X-ray photoelectron spectroscopy (XPS) was performed using a Thermo Scientific Escalab 250 Xi XPS spectrometer to evaluate the chemical composition of the samples and the oxidation states of the elements. Monochromatic *Al-*K_α X-rays and a flood gun were used to irradiate the samples and neutralize the charging effects. Ar^+ ion bombardment of the samples was performed in an XPS UHV chamber by applying an acceleration potential of 3 kV for 30 s. A survey scan was performed to assess all the elements present. The Zn 2p, O 1s, Tb 3d, and C 1s high-resolution (~ 0.5 eV) XPS spectra were acquired. The base pressure in the chamber was originally 1×10^{-8} Pa but decreased to ~ 1×10^{-4} Pa during ion bombardment. The best practice for calibrating the energy scale recently reported by Greczynski et al. [12] is to use the binding energy of the carbon C 1s peak at

(289.58 - ϕ_{ZnO}) eV , where ϕ_{ZnO} is the undoped ZnO work function. Unfortunately, we do not have a UPS installed on our instrument; therefore, we used the work function of 4.85 eV found in the literature [13]. However, for the Tb-doped samples, we looked carefully in the literature for the value of the work function of our samples but did not find any. Because the Tb content of the doped samples was less than 5%, we expected that the function would not change significantly. Therefore, we used the value for the un-doped ZnO. Experiments were repeated to verify the reproducibility of the results. The dedicated software "Avantage" (Software integrated in Thermo Scientific XPS instrument) was used to fit the experimental data. The sample structure was investigated by X-ray diffraction (XRD) using *Cu-*K_α radiation (λ=1.5406 Å) with a Rigaku Ultima-IV X-ray diffractometer. UV-Visible spectrophotometry using a Shimadzu SolidSpec-3700DUV and photoluminescence (PL) experiments using the 325 nm line excitation from a He-Cd laser and a 405 nm diode laser were carried out to investigate the optical properties. The current-voltage *(I-V)* characteristics of the prepared samples were measured using voltammetric techniques (in our case, linear sweep voltammetry) in Palmsens4 instruments.

3 Results and discussions

3.1 Terbium incorporation

The Tb concentration (X_{Tb}) and its distribution in the prepared samples were studied using EDX (mapping and spectra). X_{Tb} incorporated in the ZnO host was calculated from the Tb and Zn atom concentrations, measured at three positions and in a small selected area, by the ratio *Tb%/(Tb%+Zn%)* [14]. The average values for our samples *Y* wt % Tb-ZnO (where *Y* represents the Tb weight percentage used in the preparation of the CBD solution) are given in Table 1. The stable oxidized form of terbium takes a value of +3, but one can also find the form +4. The standard potential difference

between the trivalent and quadrivalent form is 3.1 V [15]. This standard potential shows that it is the trivalent form, which is the most stable. This indicates that the terbium does not change the valence when inserted into the ZnO matrix. The differences in the radii of Zn^{2+} (74 pm) and Tb^{3+} (92 pm) [15] indicate that the substitution doping hypothesis is only valid for low doping rates. Thus, it is probable that this trivalent state favors the segregation of dopants by a certain percentage. Although 25 wt % of terbium III nitrate pentahydrate was dissolved in the prepared solution, the maximum Tb incorporation in our sample, as obtained by EDX, did not exceed 4.2% but higher than obtained for Eu dopant [11]. As seen in Table 1, the concentration of Tb incorporated in ZnO increases with the annealing temperature, which can be caused by the diffusion of segregated Tb ions in the volume of the ZnO microstructure. The distribution of Tb ions in our samples was observed by EDX mapping for each element present in the sample. For illustration, element's EDX and element overlap maps scanned on a (5 μm ×5 μm) area of the surface sample for 5 wt % Tb-doped ZnO sample as grown (X_{Tb} = 0.80%) and that of 25 wt % Tb-doped ZnO annealed at 700 ° C (X_{Tb} = 4.21%) are shown in Fig. 1 (a) and (b) respectively. As seen by EDX maps, ZnO microstuture does not completely cover the substrate surface but differs from sample to another and from one area to another. The concentration of Tb incorporated in the samples was not uniform.

3.2 Sample morphology

Fig. 2 shows the SEM images of all the as-grown samples and those heated at 300, 500, and 700 ° C. The micropod shape of the ZnO microstructure was observed by SEM. We can distinguish micropods with two (bipods), three (tripods), and cross-linked structures with many arms. The silicon substrate seems to be just a support for these micropods, which have different sizes. The large one can reach 2 μm in length

and 1 μm in diameter. They have a perfectly hexagonal shape with very smooth sidewalls. For $T_a \geq 500$ ° C, obscure tasks appeared in the micropods, which were clearer and larger as the annealing temperature increased. They reflect the appearance of structural defects caused by evacuation from the precursor solution [2] and the recrystallization process during heat treatment. The growth mechanism of this ZnO morphology was reported by Gokarna et al. [16].

3.3 Chemical analysis

Terbium is one of the few rare earths that have a +4 and +3 oxidation state; the former is a result of the stability of the half-filled 4f shell. To explore the oxidation state of the incorporated Tb ions in our sample, XPS analysis was performed for the un-doped and 25 wt% Tb-doped ZnO micropods on Si substrate as grown and annealed at 300, 500 and 700 ° C. The C 1s BE was set to 284.73 eV, and all other core levels were aligned accordingly. The wide-scan XPS survey spectra and those of the Zn 2p, O 1s and Tb 3d core levels are shown in Fig. 3. All peaks within the survey spectra were assigned to the core levels of Zn, Si, O, C, and Tb, according to the XPS handbook [17]. However, iron (Fe) impurities are present in the doped samples. This may have been caused by the residual rust of the forceps used to fix the substrate in the chemical bath. In the XPS spectrum of the Zn2p core level, the two peaks located at approximately 1021.9 and 1044.9 eV correspond to $Zn^{2+}2p_{3/2}$ and $Zn^{2+}2p_{1/2}$. Their positions are very close to those reported in the literature (1021.9 and 1045.4 eV) [18], and they confirm the hexagonal wurtzite structure of ZnO micropods [19]. The energy difference between the two peaks (23 eV) is very close to the standard value (22.97 eV), confirming the existence of Zn^{2+} ions [20]. As the annealing temperature increases, a shift to high energy appears for the un-doped sample caused by a perturbation of bonding energy induced by the increase in structural defects, as

confirmed by the SEM image. This shift was not observed for 25 wt % Tb-doped ZnO. Therefore, the perturbation induced by structural defects is counterbalanced by that caused by the incorporation of Tb ions into the ZnO matrix. The XPS spectra of oxygen 1s peak shown in Fig. 3 are a broad and asymmetric peak for the different annealing temperatures, suggesting the existence of more than one component. The individual components were extracted after deconvolution using multiple Gaussian peaks (Fig. 4). The Gaussian fitting of the O1s XPS spectrum of un-doped ZnO micropods gives three peaks situated at approximately 528.6, 530.5 and 532.5 eV. The first one labeled O_1 in Fig. 4 corresponds to the O^{2-} ion forming bonds with Zn^{2+} ions (O-Zn groups) in the wurtzite structure of ZnO [21]. The second peak, referred as O_2 in Fig. 4, is related to the O^{2-} ions inserted in the oxygen-deficient ZnO structure (O-deficient groups). The peak O_3 at approximately 532.5 eV is attributed to the O-H groups in the surface-absorbed oxygen as CO_2 and/or H_2O [22,23]. For 25 wt % Tb-doped ZnO, the O 1s peak became broad and asymmetric at different annealing temperatures, suggesting the existence of various components. These peaks were deconvoluted with four Gaussians, among which the positions of the three peaks were very close to those obtained for the un-doped sample. However, the fourth weak and broad peak located around 526 eV may be attributed to the H–ZnO $(10\bar{1}0)$ surface, as reported by Kotsis and Staemmler [23] using ab initio calculations. They showed that the binding energy of oxygen from H–ZnO $(10\bar{1}0)$ surface was 529 eV. The result of O 1s peak deconvolution (Fig. 4) shows a significant change in the intensity and the full width at half maximum (FWHM) for each component as a function of Tb concentration and annealing temperature. The details (peak position, intensity, and area ratio) of the O 1s components for the un-doped and doped ZnO micropods as grown and annealed at different temperatures are listed in Table 2. For the un-doped

sample, O-deficient groups dominated at low annealing temperatures (≤ 300 ° C) and decreased at higher annealing temperatures. Thus, more oxygen vacancies are filled by free oxygen atoms outside the wurtzite structure and are converted to O-Zn groups. This was explained by Jiang et al. [24] by an enlargement of the atom spaces in the wurtzite structure and/or by increasing the dynamic energy of the atoms at high annealing temperatures. Compared to the as-grown doped ZnO, the area ratio percentage of O_1 and O_3 peaks (corresponding to O-Zn and O-H groups, respectively) decreased and that of O-deficient groups (O_2 peak) increased for the samples annealed at 300 ° C and 700 ° C. The decrease in the O_3 peak can be attributed to the removal of surface contaminants or the conversion of O–H groups to O deficiency. A possible reason for the decrease in O-Zn groups is the appearance of defect oxygen [25] as T_a increases. However, these observations were not verified for the sample annealed at 500 ° C, the intensity of the O_3 peak is higher may be due mostly to more surface-adsorbed oxygen species and/or the presence of structural defects in ZnO micropods, as confirmed by SEM, rather than the increase in Tb concentration. The XPS spectra of the Tb 3d level for 25 wt % Tb-doped ZnO as grown and annealed clearly reveal the presence of Tb $3d_{3/2}$ and Tb $3d_{5/2}$ peaks positioned at approximately 1277 and 1241 eV, respectively, with an asymmetric satellite peak at around 1250 eV. The positions of these peaks are very close to those reported in the literature [26,27]. The spin–orbit splitting was estimated to be 35 eV. The positions of these peaks are shifted from those for pure $TbO_{1.5}$ (Tb^{3+}), where the Tb $3d_{3/2}$ and Tb $3d_{5/2}$ peaks are located at approximately 1274 (satellite peak at 1286.3) and 1239.1 (satellite peak at 1250.4) eV [28]. The Tb $3d_{3/2}$ XPS peak and the satellite peak at 1250 eV appear to be an overlap of two peaks, which indicates the presence of two chemical states of Tb. This might be caused by the oxidation of trivalent Tb^{3+} into Tb^{4+} when bombarded by

a high-energy photoelectron and/or their effective insertion inside the ZnO host. In fact, tetravalent Tb^{4+} is observed in the commercial terbium oxide $TbO_{1.82}$, and has a binding energy of 1241.4 eV, which is slightly higher than that in Tb_2O_3 (1241.2 eV) and a satellite peak at 1251.4 eV [28]. Therefore, each XPS peak of the Tb 3d level for the 25 wt % Tb-doped ZnO was deconvoluted into two components, and the results are shown in Fig. 5. According to Zhao et al. [28], the second peak may be attributed to Tb^{4+}. Fig. 5 and Table 3 present the details of the XPS deconvoluted peak obtained for the 25 wt % Tb-doped ZnO micropods as grown and annealed. The literature peak positions of the other terbium compounds are listed in Table 3 for comparison. The position of the different deconvoluted peaks are very close to that reported in literature except the weak satellite peak (number 7) around 1283.3 eV which present a relatively high shift compared to Tb $3d_{3/2}$(4+) for $TbO_{1.82}$. Thus, we conclude from the present XPS results that Tb was found in two oxidation states (3+, 4+) in the micropod ZnO. In our preparation of the chemical solution for the doped samples, we fixed the Tb/Zn ratio. In order to be able to compare dopant concentration obtained by EDX, to that estimated by XPS measurement, the composition of Tb^i (i=+3 or 4+) is calculated from the XPS curves using the following equations:

$$C_{Tb^i} = \frac{(A_{Tb^i} / S_{Tb})}{((A_{Tb^{3+}} + A_{Tb^{4+}}) / S_{Tb}) + (A_{Zn^{2+}} / S_{Zn})} \qquad (1)$$

where A_x and S_x represent the XPS spectral area and the sensitivity factor (RSF) of element x taken from the library available with the instrument fitting software (Avantage). The calculated Tb^{3+} and Tb^{4+} concentrations for the 25 wt %-doped ZnO micropods are listed in Table 4. A good agreement was observed between the weight percentage using the prepared chemical solution and the sum of the two Tb oxidation

state concentrations. These quantitative analyses indicated that the most important quantity of Tb incorporated in ZnO micropods was in the trivalent form, and their concentration increased with the annealing temperature. Although the sample composition can be obtained using both XPS and EDX techniques, the main signal in XPS comes from a few atomic layers at the surface (a few nanometers), but the total area analyzed by EDX can reach a few micrometers. Thus Tb atomic concentrations estimated by EDX rather present the "bulk" concentration in a sample however XPS value gives the near surface region chemical composition.

3.4 Structure analysis

To confirm the phase composition and crystallinity of the synthesized Tb-doped micropods, XRD was performed (Fig. 6). The indexation of the different peaks was labeled in the XRD pattern. The X-ray spectra of all samples show a superposition of the ZnO micropods and substrate peaks. The peaks observed at 32.94° correspond to the diffraction from the (002) plane of the Si substrate. The other peaks are indexed to the wurtzite ZnO structure and match the values of the standard card for zincite ZnO (JCPDS No. 36-1451). However, the XRD spectra for X_{Tb} = 1.72 % (T_a = 300 ° C) and for X_{Tb} = 1.60 % (T_a = 700 ° C) show a weak peak around 43.5° corresponding to terbium hydroxide ($Tb(OH)_3$) or terbium oxide (Tb_2O_3). A slight shift in the peak positions was observed for the doped XRD pattern compared to that of the un-doped sample. A preferential orientation along the axis [100] is manifested for our micropods, contrary to what is reported in the literature ([101] for powder, [002] for thin films [29,30], and nanorods [31]) but similar to Eu-doped ZnO micropods [11]. The dimensions of the crystallite that form our micropods is determined using the Debye-Scherrer equation [33]:

$$t_{DS}(hkl) = \frac{k\,\lambda}{\beta_{hkl}\,cos(\theta_{hkl})} \qquad (2)$$

where $t_{DS}(hkl)$ is the crystallite size in the direction perpendicular to the lattice planes, h, k, and l are the Miller indices of the planes being analyzed, k is a numerical factor frequently referred to as the crystallite-shape factor, λ is the wavelength of the X-rays, β_{hkl} is the full width at half-maximum (FWHM) of the X-ray diffraction peak in radians, and θ_{hkl} is the Bragg angle. In our work, we used k=0.9, as reported for nanorods by Arda [33]. The SEM image of our sample showed a hexagonal shape of the micropods, which grow along the c-axis normal to the [001] direction. As the preferential orientation revealed by XRD is [100], the majority of micropods appear to precipitate from the solution on the Si substrate, orienting their flat plane (100) longitudinally. This can be explained by the relatively small mismatch between the silicon lattice parameter (a = 5.43 Å) and that of ZnO (c = 5.20 Å) and/or the low surface free energies of the (100) plane. We can assimilate the crystalline size estimated by the Debye-Scherrer equation from the (002) and (110) planes to the length and diameter of the crystallite forming the micropods [34]. For each crystallographic plane *(hkl)*, the dislocation density *(δ)*, which represents the amount of line defects, can be deduced by [34]:

$$\delta_{DS}(hkl) = \frac{1}{t_{DS}^2(hkl)} \tag{3}$$

The crystallite sizes and dislocation densities of our sample and those of the commercial powder are given in Table 5. Unlike ZnO powder, whose crystallite sizes obtained along the two crystallographic planes are nearly equal (~30 nm), confirming the spherical symmetry of the crystallite shape, that of the doped sample differs and no monotonic change is seen as a function of terbium concentration. To explore the evolution of lattice distortion as function of the Tb concentration, lattice parameters 'a', 'c', the nearest-neighbor bond lengths along the c-direction (expressed as b) and

off *c*-axis (expressed as b_1) are calculated for our sample and listed in Table 6 using respectively the following equation [35,36]:

$$d_{hkl} = \left(\frac{4}{3} \frac{h^2 + h.k + k^2}{a^2} + \frac{l^2}{c^2} \right)^{-1/2} \quad (4)$$

$$b = c\,u \text{ and } b_1 = \sqrt{\frac{1}{3}a^2 + \left(\frac{1}{2} - u \right)^2 c^2} \quad (5)$$

where d_{hkl} is the interplanar spacing, and u is the internal parameter, calculated as:

$$u = \left(\frac{1}{3} \right) \left(\frac{a}{c} \right)^2 + \frac{1}{4} \quad (6)$$

The (*c/a)* ratio and cell volume are also presented in Table 6. For our sample, the lattice parameter is slightly lower than that for ZnO powder without a monotonic variation as the concentration of Tb increases [37]. Therefore, the wurtzite structure of our micropods remains stable, which is proven by the absence of a significant change in the ratio (*c/a*) and the internal structural parameter *u*. In fact, their values are in good agreement with those determined by theoretical calculations and experimental techniques [38]. This suggests that Tb^{3+} ions go to interstitial sites in the ZnO lattice instead of substituting Zn^{2+}, inducing a slight lattice deformation caused by the dissimilarity of ionic radii and electronegativity amongst Tb (1.1) ion and Zn (1.65) as larger electrostatic forces act between them [15]. The location of the Tb ion at the interstitial site distorts the four tetrahedral bonds and has an effect similar to that of a high pressure [39].

3.5 UV–visible reflectance analysis

Because the silicon band gap is lower than that of zinc oxide, reflectance spectroscopy measurements are a suitable method for determining the energy band gap (*Eg*) of our samples. It was conducted in the ultraviolet–visible region from 300 nm to 600 nm.

The detailed optical band gap determination from reflectance spectra is detailed in our recent paper [35], and the corresponding values are listed in Table 7 as a function of Tb concentration and for the different annealing temperature. It is clear that the estimated band gap energies do not vary significantly, as seen for Eu doped ZnO [11], compared to the un-doped sample and with increasing Tb concentration. Some previous studies reported an increase [40] and a decrease in the band gap [26]. Thus, the distortion induced by the incorporation of Tb ions did not significantly affect the band gap of ZnO.

3.6 Photoluminescence study

Fig. 7 shows the PL emission (λ_{exc} = 325 nm) obtained from our Tb-doped ZnO micropods as grown and annealed at 300, 500 and 700 ° C. All samples exhibited two emission bands. A sharp ultraviolet (UV) emission band was observed at an average wavelength of 384 nm (~3.23 eV) (Table 7) and broader visible emissions spanning 420–800 nm. UV emission is recognized as the near-band-edge (NBE) transition and broad emission as deep-level emission (DLE) [41]. Un-doped ZnO is commonly attributed to intrinsic defects (Zn_i, V_O, and O_i) in ZnO [42]. The position of the UV emission peak for the un-doped sample was close to that reported by Otieno et al. [43]. A weak shift (≤10 nm) to a higher wavelength was observed for the doped sample annealed at 300 ° C and 500 ° C compared to the other samples. However, its positions were practically unchanged at a constant annealing temperature, and as the Tb concentration increased. The intensity of the UV emission differs and becomes sharper for the samples at 300 ° C and 500 ° C. An emission band at a higher energy of the NBE as a shoulder around 375 nm (~3.306 eV) appears for doped ZnO micropods annealed at 700C (Fig 6 d inset), which can be assigned to the recombination of free excitons (FX_A) [16]. This proves the better atomic

rearrangement during the crystallization of the ZnO micropods. In addition, the intensity ratio of the UV peak to visible (I_{UV}/I_{vis}) was higher for the sample annealed at 300 °C. A lower intensity ratio indicated a higher amount of defect sites inside the sample. The incorporation of Tb into the ZnO matrix and heat treatment significantly changed the visible emission band, which widened and shifted its ~~center of gravity~~ mean. This can be explained by the diffusion of Tb ions deeper into the ZnO micropod volume, which modifies defect levels within the band gap and/or change the amount of structural defects due to the presence and evaporation of the residual precursor solution during heat treatment. Direct (resonant) excitation of Tb^{3+} through f–d transitions, as reported by Kumar et al. [26] for ZnO:Tb^{3+} nanophosphors synthesized by a solution combustion method, does not appear clearly in the PL spectra. In fact, no sharp emission peaks at a single excitation are superposed or clearly protrude from the deep-level emission in the luminescence spectra of our samples. We suspect the presence of some low emissions in the PL spectra of samples grown and annealed at 700C where positions are very close to the 4f → 5d transition. This indicates a possible weak energy transfer between the ZnO host and Tb ion. Fig. 8 shows the PL spectra of the Tb-doped ZnO micropods as grown and annealed at 700 ° C when excited at a wavelength of 405 nm, which is nonresonant with the RE dopant and below the conduction band of ZnO. We detected a broad PL band in the 450–650 nm spectral range and an intensity emission peak for the grown and annealed at 700° C samples with 1.26%, 1.35%, and 1.87% Tb concentrations. These peaks correspond to $^5D_4 \rightarrow {}^7F_i$ (i=4,3) related to the Tb energy levels. Pl measurements with laser excitation wavelengths (≈488 nm) must be conducted to highlight the possible resonant levels of the dopant [37]. The terbium ions incorporated in our sample were found in mixed valence (3+ and 4+), as confirmed by XPS analysis. The extinction of

the PL intensity of the terbium ion is possibly induced by non-radiative resonant energy transfers [44] between the Tb^{3+} ions owing to their approximation. They excite each other and increase the probability of nonradiative recombination. The existence of the Tb^{4+} ion has also been mentioned by some authors [45] as the cause of this extinction. These ions of valence +4 are known in the literature to not lead to a radiative emission and may be responsible for the disappearance of the luminescence of Tb^{3+} linked to its charge and strong band of absorption in the visible region. The luminescence extinction of the transition metal can also be explained by the modification of the selection rules due to the symmetry loss of the site where the terbium is located, and therefore of the crystalline field perceived by the ion. The structural distortion induced by the incorporation of Tb in ZnO micropods seems to modify the surrounding environment of the site on which the ion is located more than that induced by Eu, as the 4f–4f transition emission have been observed in the PL spectra of Eu-doped ZnO micropods [11]. In fact, emission at 615 nm occurs [46,47] if the symmetry of the Eu site has an anti-symmetric inversion center. The intensities of the Tb emission transitions were moderately affected by the chemical environment and coordination nature of the complexes [48]. However, the lack of efficiency energy transfer between ZnO and rare earth ions or from defects towards the dopants is due to the large mismatch between the ionic radii and valence states of Zn^{2+} (74 pm) and Tb^{3+} ions (92 pm). Furthermore, the location of the rare earth ions in the host, on the surface or grain boundaries, and their diffusion as the annealing temperature increases also affects the efficiency of the energy transfer. It appears that the surrounding environment of rare-earth ions is affected inside the ZnO micropod morphology, inducing a low luminescence efficiency of Tb^{3+}. In contrast, when incorporated into thin films [43], nanoparticles/pyramids [37], nanocones [49] and nanorods [50]

morphologies, highly efficient energy transfer from RE ions via a resonant mechanism has been reported. The widening and deformation of the visible band with increasing Tb concentration and annealing temperature is due to the superposition of many different defect emissions perturbed by the presence of Tb. In fact, the native defects in ZnO, which exist as charged states or neutral, may form clusters with other intrinsic defects as well as with Tb ions [51]. We also note that the defect formation energies at the surface are lower than in bulk, and the high surface-volume ratios for our micropods result in an increase in the surface defect concentration, which could affect the ZnO visible emission [52]. The charge imbalance of Tb ions inside ZnO causes local negative charge defects, such as interstitial O and Zn vacancies. Consequently, local positive charge defects inevitably occur. This is shown by the variation in the XPS area ratio of the O-deficient groups with increasing Tb concentration and annealing temperature (Table 2). Therefore, the density defects will change by generating new and/or perturb energy levels in the band gap of ZnO, which causes the deformation of the visible emission band and, therefore, the emission color of the sample. The PL spectrum excited at 405 nm for 1.48% Tb-doped ZnO as grown is distinguished from the other spectra (Fig. 8 a) by two emission bands centered at approximately 440 and 470 nm. These blue emissions have been ascribed to the electron transition from CB to zinc vacancies V_{Zn} or oxygen antisites O_{Zn} [52,53]. The possible presence of $^5D_4 \rightarrow {}^7F_3$ peaks (at 444 nm) related to Tb energy levels cannot be affirmed as the defect emission overlays it. The transition hypersensitivity (sensitivity to the surrounding environment) of rare-earth ions is very low compared to that of organic-based fluorophores [54], and is a major inconvenience for white-light-emitting diodes when co-doped ZnO micropods with Eu and Tb. The chromaticity coordinates (x,y) for our samples were calculated using CIE color

software and the intensity data of the PL emission spectrum excited at 325 nm within 380 nm-750 nm. The corresponding coordinates are summarized in Table 8, and their positions in the CIE 1931 chromaticity diagram are presented in Fig. 9. The calculated CIE color coordinates for the un-doped sample as grown were close to those reported by Kumar et al. [26]. However, with an increase in the annealing temperature, the *x*-coordinate decreases and the *y*-coordinate decreases for T_a=300 ° C and then re-increase at 500 ° C and 700 ° C. The color coordinates were found to be in the orange yellow region for the as-grown and annealed 500 ° C ZnO micropods and in the yellowish-pink region for those annealed at 300 ° C. The chromaticity coordinates for samples annealed at 700C with X_{Tb}= 0% and 3.3% fall in the yellowish-green region. As the Tb concentration increases, the color coordinates (*x,y*) for the sample as grown and annealed at 500 ° C and 700 ° C gets closer and closer to the yellowish-green region. However, for Tb-doped ZnO annealed at 300 ° C, the color coordinate shifts to the standard D65 day light with coordinates of *x*=0.3129 and *y*=0.3292 [26]. A near-white light was achieved for Tb^{3+} concentrations higher than 1.40% and annealed at 300 ° C. Among the samples studied, green emission was obtained for un-doped and doped ZnO micropods with X_{Tb}=3.30% annealed at 700° C. This annealing temperature is more suitable for obtaining the desired green emission color, as shown in Fig. 9 a, which represents the CIE chromaticity diagram of un-doped ZnO micropods. However, heat treatment at 300° C is rather more favorable for the doped sample, as shown in Fig. 10 b for $X_{Tb} \approx 1.44\%$ and Fig. 10 c for $X_{Tb} \approx 1.70\%$. The quality of color sample emission in terms of color correlated temperature (CCT) was calculated using the McCamy empirical formula [26]:

$$CCT = -437 \times n^3 + 3601 \times n^2 - 6861 \times n + 5541.31 \quad (7)$$

where $n=(x-x_e)/(y-y_e)$ and x_e=0.3320 and y_e=0.1858 are the epicenter chromaticity coordinates. The CCT values of the samples were calculated and are summarized in Table 8. CCT values higher than 5000 K (i.e., cool CCTs) were obtained for samples in which their chromaticity coordinates were located nearest to the green region. They are appropriate for working and shopping centers [55]. The other samples have CCT values less than 5000 K (i.e., warm CCTs), which are suitable for public and living areas.

3.7 Current-voltage measurements

The *I-V* curve, conducted at room temperature and in the dark, of Tb-doped ZnO micropods on a *p*-Si substrate as grown and annealed at 300, 500 and 700 ° C for 2 h are shown in Fig. 11. All I–V characteristics are nonlinear and asymmetric, showing rectifying diode-like behavior. The I-V curve is the average signal of the area considered, and as the micropods are not uniformly dispersed on the Si surface, the current intensity does not vary monotonously as a function of X_{Tb}. This also affects the rectification ratio (I_F/I_R) (Table 9), which was calculated at ±4V in our case. Thus, the obtained values varied from one sample to another. It reached ≈ 89 for X_{Tb}=1.70% and 30 for X_{Tb} =4.21%. Unfortunately, to our knowledge, no analog electrical study has been published that would allow the comparison of our results with the literature data. The weak values of the rectification ratio and their variation from sample to other are also due to the non-saturating behavior of the reverse current, as seen in the *I-V* characteristics, which is attributed to the barrier inhomogeneities at the ZnO micropods/*p*-Si interface. When the reverse bias is increased, a greater current flows through the lower barrier height regions [56,57]. The other electrical parameters are determined considering the thermionic emission (TE) model [58] of charge transport across the heterojunction, where the current-voltage relation of a *p-n* junction is

usually written as a function of the applied voltage (V) given by the following equation [58]:

$$I = I_s\left[exp\left(\frac{q(V - IR_s)}{nKT} \right) - 1 \right] \quad (8)$$

where I_s is the saturation current, q is the electronic charge, V is the applied voltage, n is the ideality factor, K is the Boltzmann constant (1.38×10^{-23} J/K), T is the absolute temperature, and R_s is the series resistance. In practice, the establishment of electrical contacts on the semiconductor generates a so-called contact resistance whose value depends on the nature of the contact, the type of metal, and the method of design. This electrical resistance adds to that of the semiconductor and causes a voltage drop in the junction. The series resistance R_s of the heterojunction is the sum of all these resistances, and it is introduced in the previous equation in series with the ideal diode. For an applied voltage $V \geq 3kT/q$, the I-V characteristic exhibits a linear variation (ohmic regime), and conduction is limited by the volume of the heterojunction. By fitting this linear portion, we obtain the R_s, which is the inverse slope, and the intersection value with the voltage axis is the turn-on (threshold) voltage (V_F). The reverse-bias saturation current (I_s) can be derived from the intercept of the straight line of *ln (I)* at V=0, as I_s is defined by [59]:

$$I_s = AA^*\,T^2\,exp\left(-\frac{q\varphi_b}{KT} \right) \quad (9)$$

where A is the surface of the diode, A^* is the theoretical constant of Richardson equal to 32 A.cm^{-2}.K^{-2} for the case of ZnO [60], and φ_b is the height of the barrier, which can be deduced from the following equation:

$$\varphi_b = \frac{KT}{q} Ln\left(\frac{AA^*T^2}{I_s} \right) \quad (10)$$

For an ideal *p-n* junction, the *n* value must be equal to 1. However, the *n* value is generally greater because of different factors as the presence of a thin oxide layer at the interface, parasite resistance R_s, and barrier height inhomogeneity. The equation that gives us the ideality factor *n* can be translated as follows:

$$n = \frac{q}{KT}\frac{d(V - IR_s)}{dLn(I)} \tag{11}$$

and extracted from the linear region slope of the *ln(I)–V* data for forward polarization. An alternative method called Cheung-Cheung could be used to estimate the electrical parameters, as derived from the *I–V* characteristics by Akay et al. [58], using the following functions [57,59]:

$$\frac{dV}{d\,ln(I)} = \frac{nKT}{q} + IR_s \tag{12}$$

$$H(I) = V - \left(\frac{nKT}{q}\right) ln\left(\frac{I}{AA^*T^2}\right) = n\varphi_b + IR_s \tag{13}$$

R_s and *n* can be determined from the slope of the *dV/d(lnI)* versus *I* plot and the axis intercept, respectively. Using the determined *n*, *H(I)* versus *I* plot shows a straight line, the slope of this plot gives the series resistance R_S, and height barrier φ_b can be determined using the equation (*H(I)*) from the *y*-axis intercept. Fig 12 shows *dV/d(lnI)* and *H(I)* versus *I* plots for the un-doped sample and X_{Tb} = 4.21% doped ZnO annealed at 700 °C. The electrical parameters for all of our heterojunctions were extracted using the two methods and are summarized in Table 9. The ideality factor and series resistance determined by the two methods differed. However, the barrier height φ_b values are close, indicating that these procedures are trustworthy and the differences in R_s and *n* may be due to the extraction of data from different regions of the forward-bias (*I-V*) plot [61]. Indeed, the presence of disorder, impurities, or, more generally, defects strongly influence the electrical properties by inducing electronic states in the

volume, at its surface, or at the interfaces of the heterojunction during its elaboration. These states affect the *I-V* characteristics differently from one voltage range to another. For our samples, the turn-on voltage differs and reaches 5.32 V. Our values are lower than those reported by Hasabeldaim et al. [20] about 10 V for another rare earth ion (3 mol % Eu) doped ZnO thin films deposited by pulsed laser deposition at different oxygen partial pressures. The ideality factor n and barrier height φ_b obtained for our doped micropods seem to be in good agreement with those reported by Akay et al. [58] (and references therein) of thin films of ZnO and those of nanorods [57] (and references therein), but our series resistance values are very high. This is due to the irregular contact at the micropod/substrate interface. Therefore, deposition of a ZnO buffer layer on the substrate before the growth of the micropods should significantly enhance the contact at the interface, thereby increasing the rectification ratio and decreasing the series resistance. It should be noted from the above that whatever one does, the introduction of undesirable states is inherent in structures of the heterojunction type, regardless of the deposition technique used. These states, which directly affect the conduction mechanisms through charge exchanges in the form of emission and recombination in the space charge zone of the different heterostructures, have led to some divergence in the electrical parameters obtained in our study. However, similar results were obtained for Eu-doped ZnO synthesized using the same process [11].

4 Conclusions

Un-doped and Tb-doped micropod ZnO were prepared using a chemical bath, deposited on a *p*-Si substrate, and were found to have a hexagonal wurtzite structure without the presence of any secondary phase, as confirmed by XRD. The EDX results confirmed the incorporation of terbium, which increased with the annealing

temperature and reached 4.21%, but their distribution was inhomogeneous in the ZnO host. The deconvolution of the Tb-3d XPS peaks and their comparison with the literature peak positions confirm the presence of two chemical states of Tb in ZnO. The micropods deposited on the Si substrate have different numbers of arms, which are hexagonal in shape with smooth sidewalls and different sizes. The preferential orientation along the axis [100], as demonstrated by XRD, shows a privileged longitudinal alignment of ZnO micropods on the Si surface due to the small lattice mismatch between the hexagonal (100) ZnO plane and the (100) plane of the Si substrate. XRD microstructure analysis demonstrated that the simultaneous presence of Tb^{3+} and Tb^{4+} in doped micropods deforms the lattice unit by changing the length and/or the tetrahedral angle bonding while maintaining the wurtzite structure. This distortion did not lead to a significant and monotonic variation in the structural parameters and band gap values of the samples doped with a concentration ≤ 4.21%. The incorporation of Tb ions with a larger ionic radius into the ZnO micropods host breaks the symmetry of the site where the terbium is located. Therefore, the selection rules change in turn, and thus do not allow the luminescence of the transition metal. However, the defects generated in the doped samples enlarged and distorted the visible emission observed in the room-temperature PL spectra. Therefore, the simultaneous presence of Tb^{3+} and Tb^{4+} significantly affected the concentration of the intrinsic defects. As these native defects are in different charged or neutral states, they may form clusters with another intrinsic defect, as with extrinsic elements causing a change in the visible emission for doped samples. No efficient energy transfer between ZnO micropods and Tb ions or from defects towards the dopants has been highlighted. A higher intensity of UV emission than the visible emission is obtained for the sample annealed at 300 ° C which can be useful for UV random lasing

applications, and the other sample can instead be used for potential solid-state lighting applications. Photometric characterization, such as the chromaticity coordinate, shows the obtaining of a color emission for as grown and annealed at 500 ° C and 700 ° C samples that shift more towards the green color as the terbium concentration incorporated in ZnO micropods increases. For samples with an X_{Tb} ≥ of 1.44% annealed at 300 ° C, near-white light was achieved, which did not arise from the combination of the main Tb emission and those of the matrix but rather from the deep-level emission deformation. Thus, using simple and low-cost growth techniques, the color emission of the prepared sample may be controlled by the Tb concentration and heat treatment. Our samples are interesting for optoelectronic applications in which they are deposited on *p*-Si substrates because the microelectronics industry is largely dominated by the use of silicon. The electrical parameters of Tb-doped ZnO/*p*-Si heterojunction are extracted from the *I–V* measurement which reveal a successful diode-like behavior for our all samples with different rectification ratio (the higher ≅ 90) and a barrier height comprised between 0.77 and 0.90 eV not great affected by the Tb concentration. However, the deposition of a ZnO buffer layer between the substrate and the micropods should significantly enhance the contact at the interface and decrease the very high series resistance obtained for the rare earth-doped samples.

Acknowledgments

The authors take this opportunity to thank the Department of Physics, College of Science at Zulfi, Majmaah University, specifically Dr. Ibrahim Shaarany, for helpful technical assistance with equipment facilities.

Conflict of interest

The authors declare that they have no conflict of interest.

References

1 D. Daksh, and Y. K. Agrawal, Rare earth-doped zinc oxide nanostructures: a review. Rev. Nanosci. Nanotechnol. **5**, 1-27 (2016).

2 Ü. Özgür, Ya. I. Alivov, C. Liu, A. Teke, M. A. Reshchikov, S. Doğan, V. Avrutin, S.-J. Cho, and H. Morkoç, A comprehensive review of ZnO materials and devices. J. Appl. Phys. **98**, 041301 (2005).

3 B. Djurisic, A.M.C. Ng, and X.Y. Chen, ZnO nanostructures for optoelectronics: material properties and device applications. Prog. Quantum Electron. **34**, 191-259 (2010).

4 M-Y. Lu, M-P.Lu, S-J. You, C-W. Chen, and Ying-Jhe Wang, Quantifying the barrier lowering of ZnO Schottky nanodevices under UV light. Sci. Rep. **5**, 15123 (2015).

5 X. M. Zhang, M. Y. Lu, Y. Zhang, L. J. Chen, and Z. L. Wang, Fabrication of a high-brightness blue-light-emitting diode using a ZnO nanowire array grown on p-GaN thin film. Adv. Mater. **21**, 2767-2770 (2009).

6 A.B. Djurisic, Y.H. Leung, K.H. Tam, Y.F. Hsu, L. Ding, W.K. Ge, Y.C. Zhong, K.S. Wong, W.K. Chan, H.L. Tam, K.W. Cheah, W.M. Kwok, and D.L. Phillips, Defect emissions in ZnO nanostructures. Nanotechnology **18**, 095702 (2007).

7 V. Kumar, O. M. Ntwaeaborwa, T. Soga, Viresh Dutta, and H. C. Swart, Rare Earth Doped Zinc Oxide Nanophosphor Powder: A Future Material for Solid State Lighting and Solar Cells. ACS Photonics **4**, 2613-2637 (2017).

8 H. Yu, L. Xia, X. Dong, and X. Zhao, Preparation and luminescent characteristic of Eu_2O_3-ZnO/(SBA-15) composite materials. J. Lumin. **158**, 19-26 (2015).

9 L. Yang, Zh. Jiang, J. Dong, A. Pan, and X. Zhuang, The study the crystal defect-involved energy transfer process of Eu^{3+} doped ZnO lattice. Mater. Lett. **129**, 65-67 (2014).

10 L. Luo, F.Y. Huang, G.J. Guo, P.A. Tanner, J. Chen, Y.T. Tao, J. Zhuo, L.Y. Yuan, S.Y. Chen, Y.L. Chueh, H.H. Fan, K.F. Li, and K.W. Cheah, Efficient doping and energy transfer from ZnO to Eu^{3+} ions in Eu^{3+}-doped ZnO nanocrystals. J. Nanosci. Nanotechnol. **12**, 2417-2423 (2012).

11 N. A. Althumairi, I. Baig, T. S. Kayed, A. Mekki, A. Lusson, V. Sallet, A. Majid, and A. Fouzri, Characterization of Eu doped ZnO micropods prepared by chemical bath deposition on p-Si substrate. Vacuum, **198** 110874 (2022).

12 G. Greczynski, and L. Hultman, Reliable determination of chemical state in x-ray photoelectron spectroscopy based on sample-work-function referencing to adventitious carbon: Resolving the myth of apparent constant binding energy of the C 1s peak. Appl. Surf. Sci. **451**, 99-103 (2018).

13 P.-C. Lee, Y.-C. Ou, R.-C Wang, and C.-P. Liu, Enhanced output performance of ZnO thin film triboelectric nanogenerators by leveraging surface limited ga doping and insulting bulk. Nano Energy **89**, 106394 (2021).

14 A. Nouria, A. Beniaiche, B. M. Soucase, H. Guessas, and A. Azizi, Photoluminescence study of Eu^{+3} doped ZnO nanocolumns prepared by electrodeposition method. Optik **139**, 104-110 (2017).

15 M. Shkir, K. V. Chandekar, M. Badria, A. A. Khan, S. A. Mohamed, and S. Hamdy, A remarkable enhancement in photocatalytic activity of facilely synthesized Terbium@Zinc oxide nanoparticles by flash combustion route for optoelectronic applications. Appl. Nanosci. **10**, 1811-1823 (2020).

16 A. Gokarna, R. Aad, J. Zhou, K. Nomenyo, A. Lusson, P. Miska, and G. Lerondel, On the origin of the enhancement of defect related visible emission in annealed ZnO micropods. J. Appl. Phys. **126**, 145104 (2019).

17 J. F. Moulder, W. F. Stickle, P. E. Sobol, and K. D. Bomben, Handbook of X-Ray Photoelectron Spectroscopy: a Reference Book of Standard Spectra for Identification and Interpretation of XPS Data, Physical (Physical Electronics, Chicago, 1995).

18 I. Ahmad, M. S. Akhtar, E. Ahmed, M. Ahmad, V. Keller, W. Q. Khan, and N.R. Khalid, Rare earth co-doped ZnO photocatalysts: Solution combustion synthesis and environmental applications. Sep. Purif. Technol. **237**, 116328 (2020).

19 U. Alam, A. Khan, W. Raza, A. Khan, D. Bahnemann, and M. Muneer, Highly efficient Y and V co-doped ZnO photocatalyst with enhanced dye sensitized visible light photocatalytic activity. Catal. Today **284**, 169-178 (2017).

20 E. H. H. Hasabeldaim, O. M. Ntwaeaborwa, R. E. Kroon, E. Coetsee, and H. C. Swart, Luminescence properties of Eu doped ZnO PLD thin films: The effect of oxygen partial pressure. Superlattices and Microstruct. **139**, 106432 (2020).

21 V. Kumar, H. C. Swart, S. Som, V. Kumar, A. Yousif, A. Pandey, S. K. K. Shaat, and O.M. Ntwaeaborwa, The role of growth atmosphere on the structural and optical quality of defect free ZnO films for strong ultraviolet emission. Laser Phys. **24**, 105704 (2014).

22 V. Kumar, H.C. Swart, O.M. Ntwaeaborwa, R.E. Kroon, J.J. Terblans, S.K.K. Shaat, A. Yousif, and M.M. Duvenhage, Origin of the red emission in zinc oxide nanophosphors. Mater. Lett. **101**, 57-60 (2013).

23 K. Kotsis, and V. Staemmler, Ab initio calculations of the O1s XPS spectra of ZnO and Zn oxo compounds. Phys. Chem. Chem. Phys. **8** 1490-1498 (2006).

24 L. Jiang, J. Li, K. Huang, S. Li, Q. Wang, Z. Sun, T. Mei, J. Wang, L. Zhang, N. Wang, and X. Wang, Low-Temperature and Solution-Processable Zinc Oxide Transistors for Transparent Electronics. ACS Omega **2**, 8990-8996 (2017).

25 A. Hastir, R. L. Opila, N. Kohli, Z. Onuk, B. Yuan, K. Jones, Virpal, and R. C. Singh, Deposition, characterization and gas sensors application of RF magnetron-sputtered terbium-doped ZnO films. J Mater Sci, **52**, 8502-8517 (2017).

26 V. Kumar, S. Som, V. Kumar, V. Kumar, O.M. Ntwaeaborwa, E. Coetsee, and H.C. Swart, Tunable and white emission from ZnO:Tb^{3+} nanophosphors for solid state lighting applications. Chem. Eng. Sci. **255**, 541-552 (2014).

27 M. Balaguer, C-Y. Yoo, H. JM Bouwmeester, and J. M. Serra, Bulk transport and oxygen surface exchange of the mixed ionic–electronic conductor Ce_{1-x} $Tb_xO_{2-\delta}$ (x= 0.1, 0.2, 0.5). J. Mater. Chem. A. **1**, 10234-10242 (2013).

28 Y. Zhao, J-G. Li, M. Guo, and X. Yang, Structural and photoluminescent investigation of LTbH/LEuH nanosheets and their color-tunable colloidal hybrids. J. Mater. Chem. C **1**, 3584-3592 (2013).

29 R. Majitha, J. Speich, and K. E. Meissner, Mechanism of Generation of ZnO Microstructures by Microwave-Assisted Hydrothermal Approach. Materials **6**, 2497-2507 (2013).

30 K. Govender, D. S. Boyle, P. B. Kenway, and P. O'Brien, Understanding the factors that govern the deposition and morphology of thin films of ZnO from aqueous solution. J. Mater. Chem. **14**, 2575-2591 (2004).

31 M. A. Vergés, A. Mifsud, and C. J. Serna, Formation of rod-like zinc oxide microcrystals in homogeneous solutions. J. Chem. Soc. Faraday Trans. **86**, 959-963 (1990).

32 I. Massoudi, T. Ghrib, A. L. Al-Otaibi, K. Al-Hamadah, S. Al-Malky, M. Al-Otaibi, and M. Al-Yatimi, Effect of Yttrium Substitution on Microstructural, Optical, and Photocatalytic Properties of ZnO Nanostructures. J. Electron. Mater. **49**, 5353-5362 (2020).

33 L. Arda, The effects of Tb doped ZnO nanorod: An EPR study. J. Magn. Magn. Mater. **475**, 493-501 (2019).

34 A. Srivastava, N. Kumar, K. Prakash Misra and S. Khare, Enhancement of band gap of ZnO nanocrystalline films at a faster rate using Sr dopant. Electron. Mater. Lett. **10**, 703-711 (2014).

35 A. Fouzri, N. Ahmed Althumairi, V. Sallet, and A. Lusson, Characterization of sol gel $Zn_{1-x}Ca_xO$ thin layers deposited on p-Si substrate by spin-coating method. Opt. Mater. **110**, 110519 (2020).

36 H. Morkoç, and Ü. Özgür, Zinc Oxide: Fundamentals, Materials and Device Technology; (WILEY-VCH, Weinheim, 2009).

37 L. F. Koao, B. F. Dejene, H. C. Swart, S. V. Motloung, T. E. Motaung, and S. P. Hlangothi, Effect Of Tb^{3+} Ions On The ZnO Nanoparticles Synthesized By Chemical Bath Deposition Method. Adv. Mater. Lett. **7**, 529-535 (2016).

38 Ü. Özgür, Ya. I. Alivov, C. Liu, A. Teke, M. A. Reshchikov, S. Doğan, Vitaliy Avrutin, S.-J. Cho, and H. Morkoç, A comprehensive review of ZnO materials and devices, J. Appl. Phys. **98**, 041301 (2005).

39 C.-M. Lin, H.-T.Liu, S.-Y. Zhong, C.-H. Hsu, Y.-T. Chiu, M.-F.; Tai, J.-Y. Juang, Y.-C. Chuang, and Y.-F. Liao, Structural Transitions in Nanosized $Zn_{0.97}Al_{0.03}O$ Powders under High Pressure Analyzed by in Situ Angle-Dispersive X-ray Diffraction. Materials **9**, 561 (2016).

40 R. Sreeja Sreedharan, R. Reshmi Krishnan, R. Jolly Bose, V.S. Kavitha, S. Suresh, R. Vinodkumar, S. K. Sudheer, and V. P. Mahadevan Pillai, Visible luminescence from highly textured Tb^{3+} doped RF sputtered zinc oxide films. J. Lumin. **184**, 273-286 (2017).

41 R. Raji, and K.G. Gopchandran, ZnO nanostructures with tunable visible luminescence: Effects of kinetics of chemical reduction and annealing. J. Sci.: Adv. Mater. Devices **2**, 51-58 (2017).

42 C. Ahn, Y.Y. Kim, D.C. Kim, S.K. Mohanta and H.K. Cho, A comparative analysis of deep level emission in ZnO layers deposited by various methods. J. Appl. Phys. **105**, 013502 (2009).

43 F. Otieno, M. Airo, R. M. Erasmus, D. G. Billing, A. Quandt, and D. Wamwangi, Effect of thermal treatment on ZnO:Tb^{3+} nanocrystalline thin films and application for spectral conversion in inverted organic solar cells. RSC Adv. **8**, 29274-29282 (2018).

44 R. K. Verma, K. Kumar, and S. B. Rai, Inter-conversion of Tb^{3+} and Tb^{4+} states and its fluorescence properties in MO–Al_2O_3: Tb (M = Mg, Ca, Sr, Ba) phosphor materials. Solid State Sci. **12**, 1146-1151 (2010).

45 A. D. Sontakke, and K. Annapurna, Study on Tb^{3+} containing high silica and low silica calcium aluminate glasses: Impact of optical basicity. Spectrochim. Acta. A. Mol. Biomol. Spectrosc. **94**, 180-185 (2012).

46 T.-H. Fang, Y.-S. Chang, L.-W. Ji, S. D. Prior, W. Water, K.-J. Chen, C.-F. Fang, C.-N. Fang, and S.-T. Shen, Photoluminescence characteristics of ZnO doped with Eu^{3+} powders. J. Phys. Chem. Solids **70**, 1015-1018 (2009).

47 M. Zhong, G. Shan, Y. Li, G. Wang, and Y. Liu, Synthesis and luminescence properties of Eu^{3+}-doped ZnO nanocrystals by a hydrothermal process. Mater. Chem. Phys. **106**, 305-309 (2007).

48 F. S. Richardson, Terbium(III) and europium(III) ions as luminescent probes and stains for biomolecular systems. Chem. Rev. **82**, 541-552 (1982).

49 Y. H. Yang, H. G. Zhu, H. M. Dong, and G. W. Yang, Growth and luminescence of Tb-doped ZnO nanocones, Mater. Lett. **124**, 32-35 (2014).

50 P. P. Pal, and J. Manam, Color tunable ZnO nanorods by Eu^{3+} and Tb^{3+} co-doping for optoelectronic applications, Appl. Phys. A **116**, 213-223 (2014).

51 G. Lakshminarayana, K.M. Kaky, S.O. Baki, A. Lira, U. Caldiño, I.V. Kityk, and M.A. Mahdi, Optical absorption, luminescence, and energy transfer processes studies for Dy^{3+}/Tb^{3+}-codoped borate glasses for solid-state lighting applications. Opt. Mater. **72**, 380-391 (2017).

52 A. Galdámez-Martinez, G. Santana, F. Güell, PR Martínez-Alanis, and A. Dutt, Photoluminescence of ZnO Nanowires: A Review. Nanomaterials (Basel) **10**, 857 (2020).

53 L. Yang, Z. Wang, Z. Zhang, Y. Sun, M. Gao, J. Yang, and Y. Yan, Surface effects on the optical and photocatalytic properties of graphene-like ZnO:Eu^{3+} nanosheets. J. Appl. Phys. **113**, 033514 (2013).

54 J. Georges, Lanthanide-sensitized luminescence and applications to the determination of organic analytes. A review . Analyst **118**, 1481-1486 (1993).

55 S. Sharma, and C. Periasamy, A study on the electrical characteristic of n-ZnO/p-Si heterojunction diode prepared by vacuum coating technique. Superlattices and Microstruct. **73**, 12-21 (2014).

56 R N Gayen, and S R Bhattacharyya, Electrical characteristics and rectification performance of wet chemically synthesized vertically aligned n-ZnO nanowire/p-Si heterojunction. J. Phys. D: Appl. Phys. **49**, 115102 (2016).

57 S. Muniza Faraz, W. Shah, N. Ul Hassan Alvi, O. Nur, and Q. Ul Wahab, Electrical Characterization of Si/ZnO Nanorod PN Heterojunction Diode. Adv. Condens. Matter Phys. **2020**, 1 (2020).

58 S. K. Akay, S. Sarsıcı, and H. K. Kaplan, Determination of electrical parameters of ZnO/Si heterojunction device fabricated by RF magnetron sputtering. Opt. Quantum Electron. **50**, 362 (2018).

59 S. O. Tan, İ. Taşcıoğlu, S. Altındal Yerişkin, H. Tecimer, and F. Yakuphanoğlu, Illumination Dependent Electrical Data Identification of the CdZnO Interlayered Metal-Semiconductor Structures. Silicon **12**, 2885-2891 (2020).

60 A. Das, A. Kushwaha, R. Sivasayan, S. Chakraborty, H. Dutta, A. Karmakar, D. Chi, G. Dalapati, and S. Chattopadhyay, Temperature-dependent electrical characteristics of CBD/CBD grown n-ZnO nanowire/p-Si heterojunction diodes. J. Phys. D: Appl. Phys. **49**, 145105 (2016).

61 Ş. Karataş, N. Yildirim, and A. Türüt, Electrical properties and interface state energy distributions of Cr/n-Si Schottky barrier diode. Superlattices and Microstruct. **64**, 483-494 (2013).

Captions for Tables

Table 1: Average concentration of terbium X_{Tb}(%) incorporated in ZnO annealed at various temperatures (T_a) determined by EDX.

Table 2: Position and area ratio of the three peaks O_1, O_2, O_3 (O−Zn groups, O-deficient groups, O−H groups) at different annealing temperatures for un-doped and 25 wt % Tb-doped ZnO micropods.

Table 3: Deconvoluted XPS peak positions obtained for the 25wt % Tb-doped ZnO micropods as function of T_a. For comparison, the literature peak positions of other terbium compounds are provided.

Table 4: C_{Tb}^{3+} and C_{Tb}^{4+} (at %) concentration obtained from XPS measurements for 25 wt % Tb-doped ZnO micropods as grown and annealed at various temperature (T_a). The sensitivity factors (RSF) used were Zn: 18.92, and Tb: 49.42.

Table 5: Debye-Scherrer crystallite sizes and dislocation density for (002) and (110) peaks as function of X_{Tb} and for the different annealed temperature (T_a). For comparison, those of commercial powder are also given.

Table 6: Cell parameters (a and c), c/a ratio , unit cell volume, u parameter , bond length b, and b_1 as functions of Tb concentration (X_{Tb}) and annealing temperature (T_a). For comparison structure parameters of the commercial ZnO powder and those of the JCPDS XRD database, file number 36–1451 are also listed.

Table 7: Band gap values of Tb-doped ZnO micropods for different Tb concentrations (X_{Tb}) and heat temperatures (T_a) obtained from UV–Vis reflectance and photoluminescence spectroscopy.

Table 8: Calculated CIE color coordinates (x,y) for Tb-doped ZnO micropods as function of Tb concentration (X_{Tb}) and annealing temperature (T_a).

Table 9: Calculated values of the rectification ratio (I_F/I_R) calculated at ±4V, turn-on voltage (V_F), reverse saturation current (I_s), ideality factor (n), barrier height (φ_b), and series resistance (R_s) for all samples using two methods.

Captions for Figures

Fig. 1: Elemental EDX and element overlap maps of 5 wt % Tb-doped ZnO as-grown (X_{Tb} = 0.80%) (a) and 25 wt % Tb-doped ZnO annealed at 700 ° C (X_{Tb} = 4.21%) (b).

Fig. 2: SEM images of Y wt% Tb-doped ZnO micropods on p-Si substrate (a) Y = 0, (b) Y = 5, (c) Y =10, (d) Y = 15 (e), Y = 20, and (f) Y=25 as grown and annealed at 300, 500 and 700 ° C.

Fig. 3: XPS binding energy spectra of (a) un-doped ZnO for the Zn2p and O1s core levels and (b) 25 wt %Tb-doped ZnO for the Zn2p, O1s and Tb3d core level as a function of the annealing temperature. The corresponding XPS survey spectra are also presented.

Fig. 4: De-convoluted O1s XPS core level spectra of (a) un-doped and (b) 25 wt % Tb-doped ZnO micropods as grown and annealed at 300, 500, and 700 ° C. The individual components were identified after fitting with multiple Gaussian peaks. The dashed wine line represents the cumulative fitting of all individual peaks.

Fig. 5: De-convoluted Tb 3d XPS core-level spectra of 25 wt % Tb-doped ZnO micropods. The individual components were identified after fitting with multiple Gaussian peaks. The dashed-dotted purple line represents the cumulative fit for all individual peaks.

Fig. 6: X-ray diffraction spectra of Tb-doped ZnO micropods on p-Si substrate as grown (a) and annealed at 300 ° C (b), 500 ° C (c), and 700 ° C (d).

Fig. 7: Photoluminescence spectra (excited at 325 nm) of Tb-doped ZnO micropods as grown (a), annealed at 300 ° C (b) 500 ° C (c), and 700 ° C (d).

Fig. 8: Photoluminescence spectra (excited at 405 nm) of as-grown Tb-doped ZnO micropods (a) and annealed at 700 ° C (b).

Fig. 9: CIE coordinate diagrams of un-doped and Tb-doped ZnO samples as grown (a), annealed at 300 ° C (b), 500 ° C (c), and 700 ° C (d).

Fig. 10: CIE coordinate diagrams of un-doped (a), 1.44% (b), and 1.70 % (c) Tb-doped ZnO micropods annealed at different temperatures.

Fig. 11: Plots of the current–voltage (I–V) characteristics of Tb-doped ZnO micropods on p-Si substrate for different Tb concentrations (X_{Tb}) (a) as grown and annealed for 2 h at (b) 300 ° C, (c) 500 ° C, and (d) 700 ° C.

Fig. 12: dV/d(lnI)–I and H(I)–I plots of the un- and 4.21% Tb-doped heterojunction samples annealed at 700° C.

Figure 1

(a)

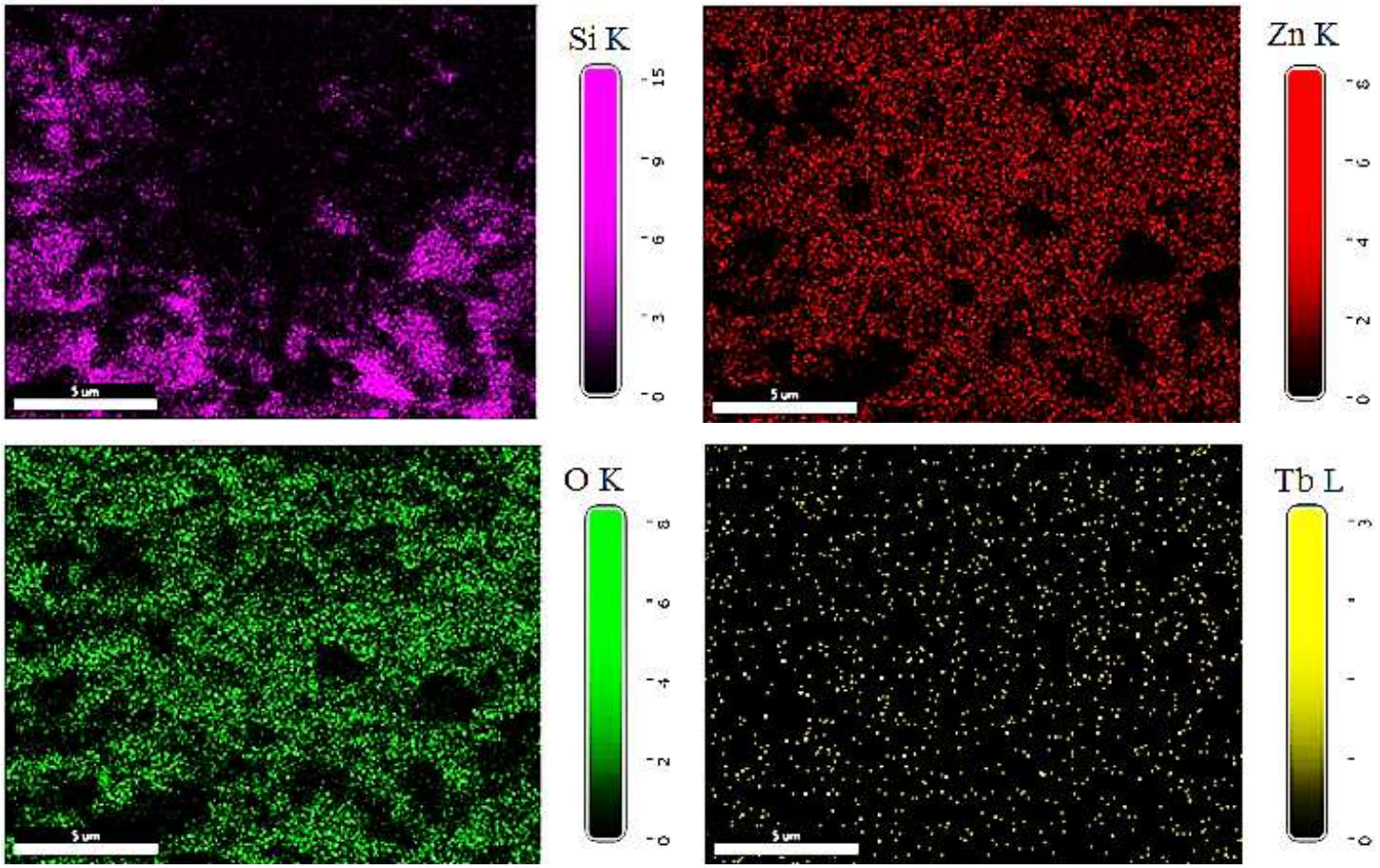

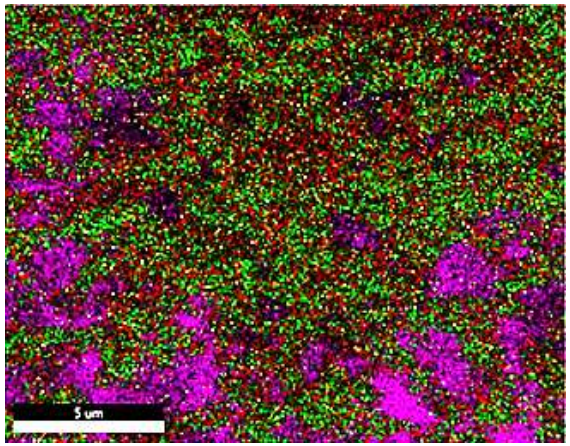

(b)

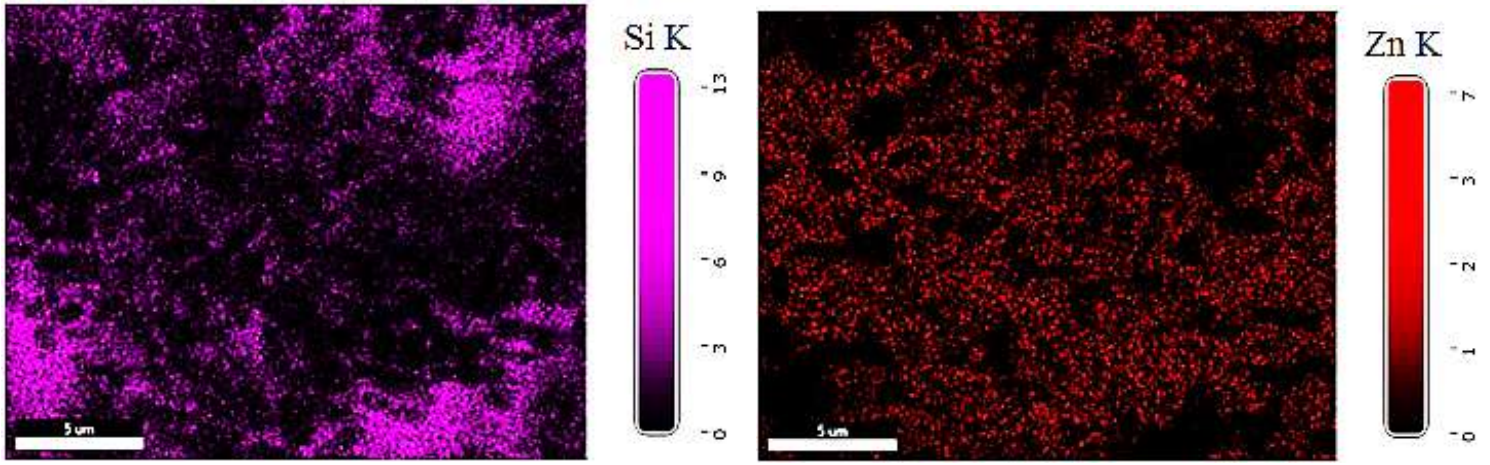

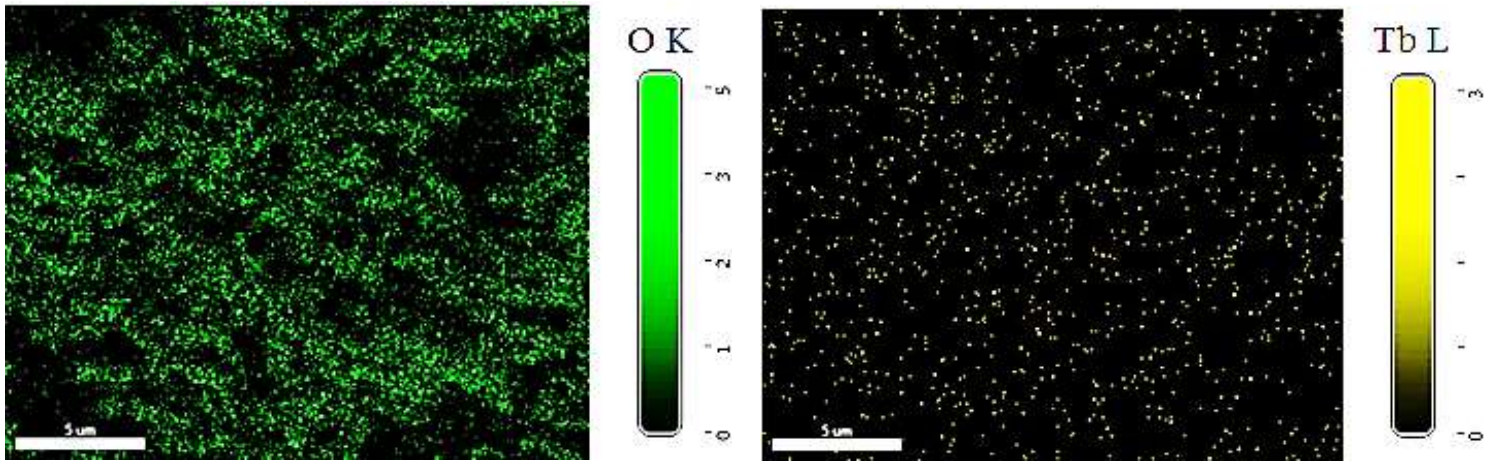
O K
5 um
Tb L
5 um
5 um

Figure 2

(a)

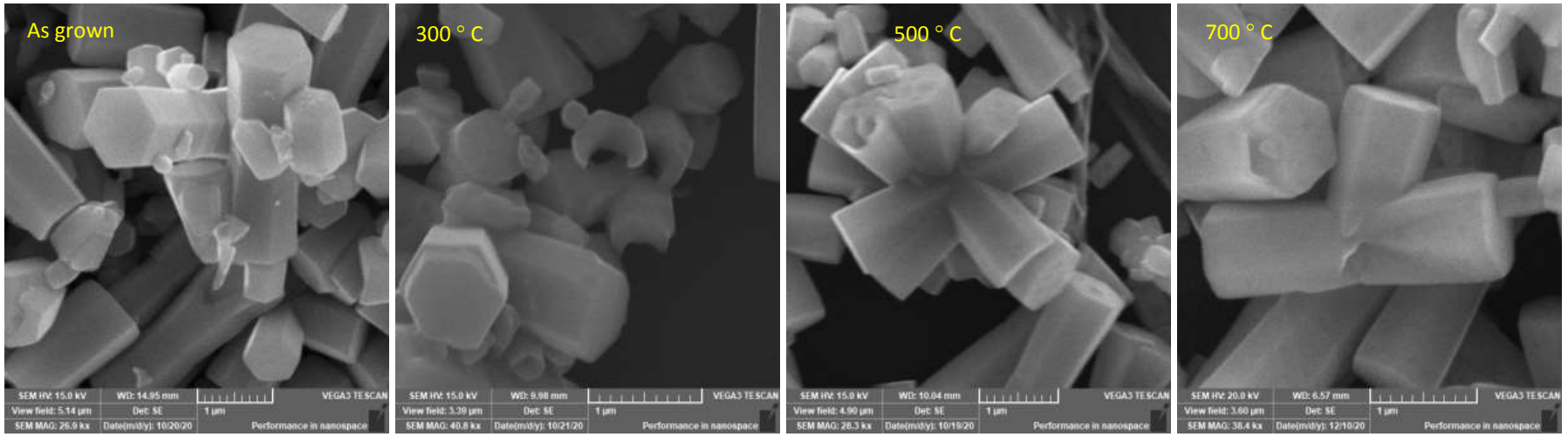

(b)

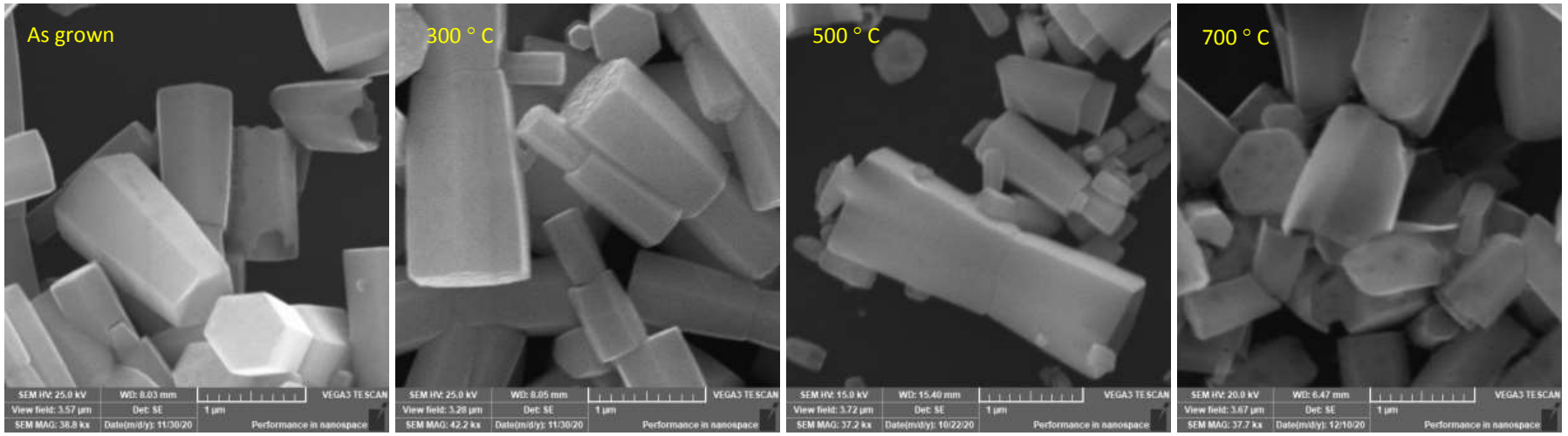

(c)

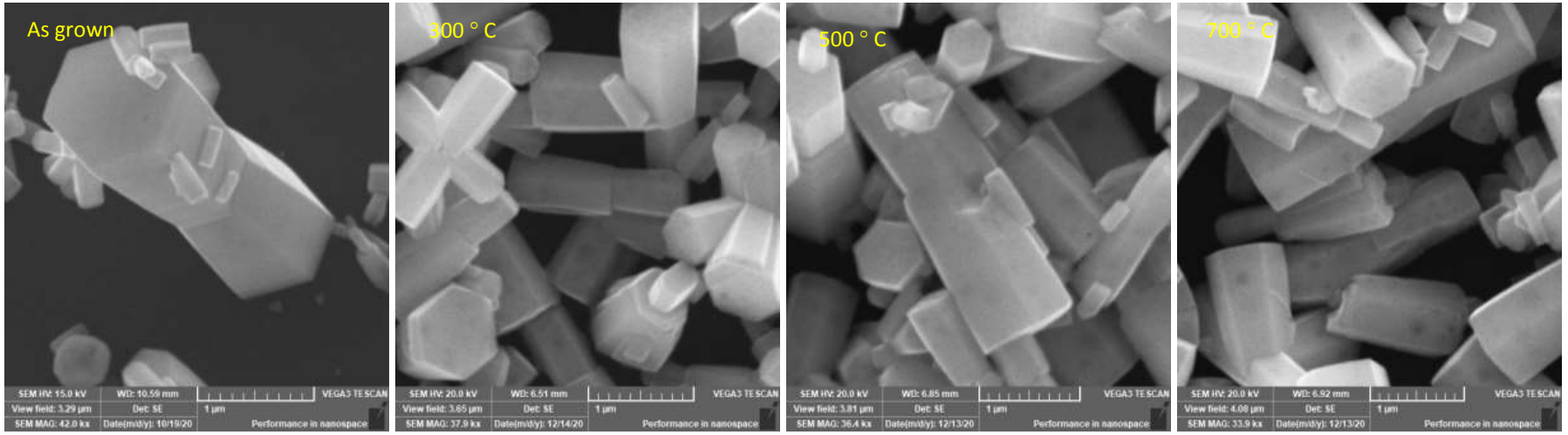

(d)

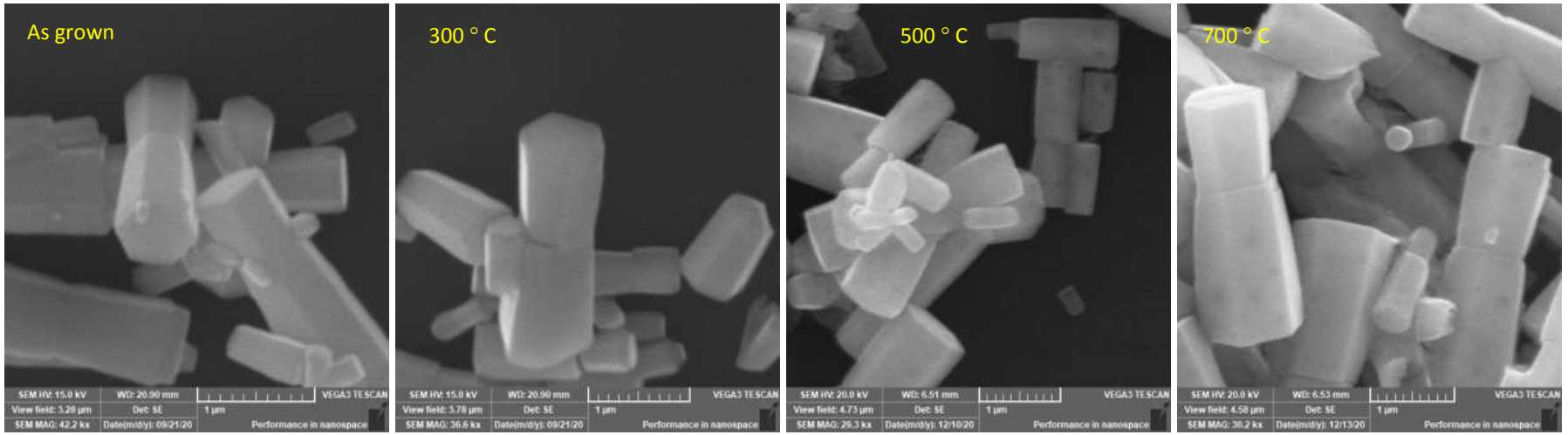

(e)

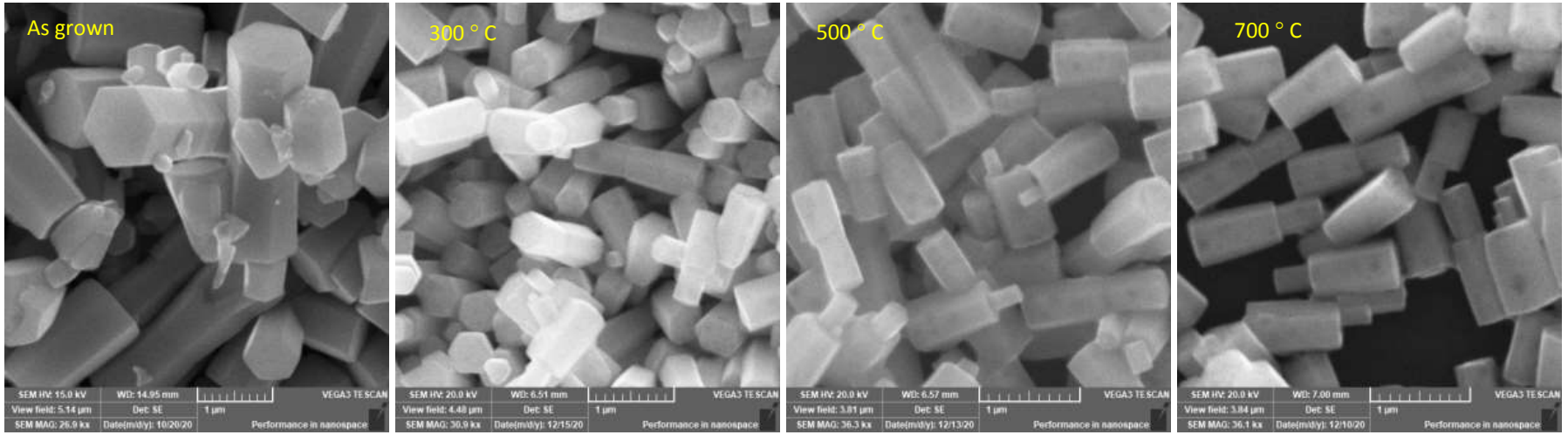

(f)

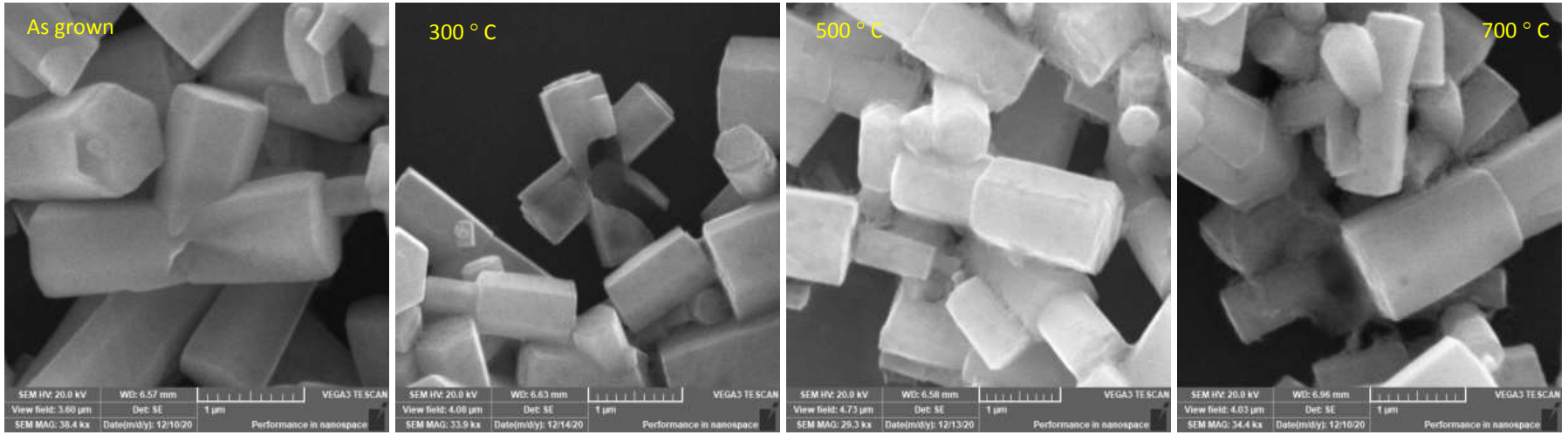

Figure 3

(a)

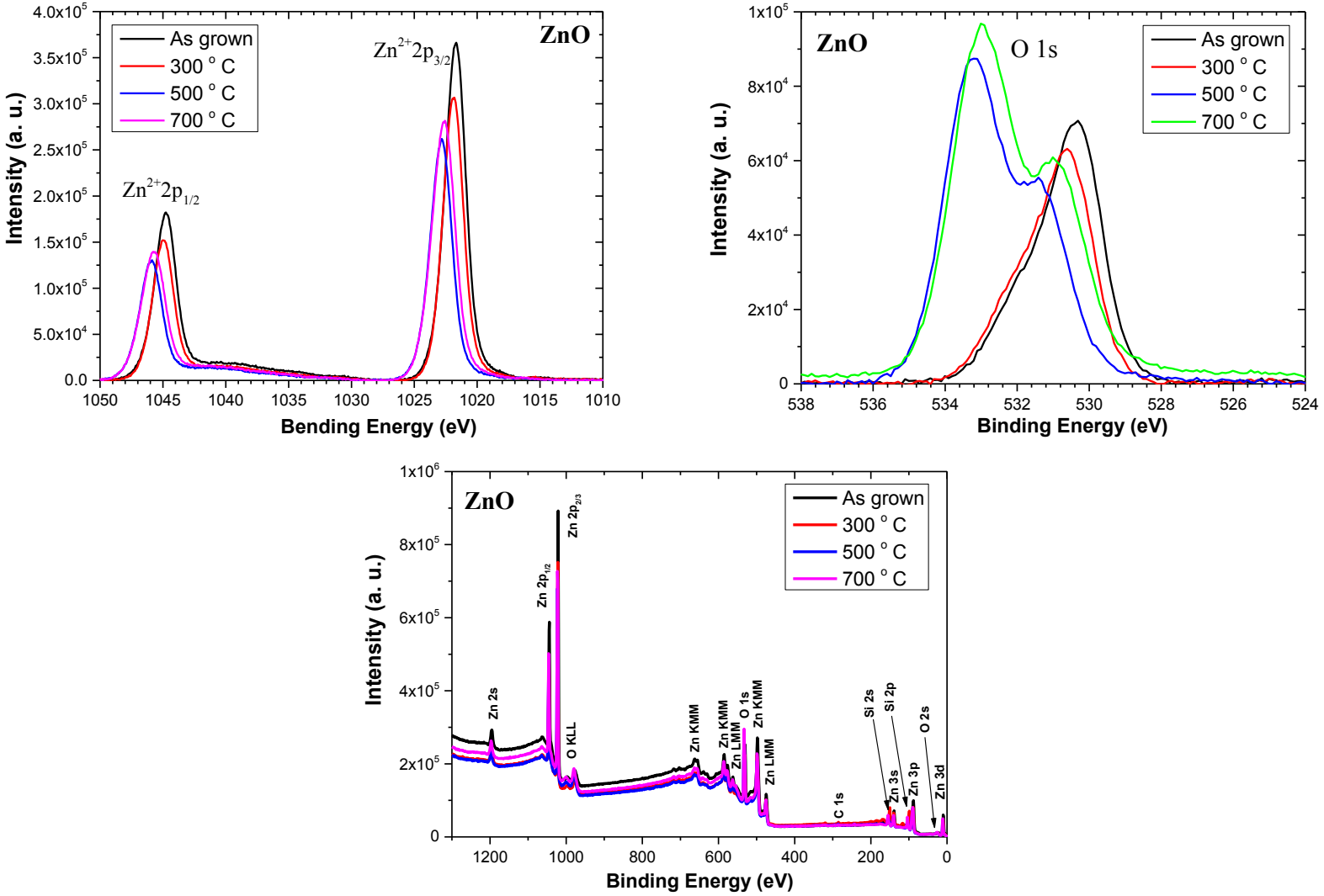
ZnO
As grown
300 ° C
500 ° C
700 ° C
Zn2+2p3/2
Zn2+2p1/2
Intensity (a. u.)
Bending Energy (eV)
ZnO
O 1s
As grown
300 ° C
500 ° C
700 ° C
Intensity (a. u.)
Binding Energy (eV)
ZnO
As grown
300 ° C
500 ° C
700 ° C
Zn 2p2/3
Zn 2p1/2
Zn 2s
O KLL
Zn KMM
Zn KMM
Zn LMM
O 1s
Zn KMM
Zn LMM
C 1s
Si 2s
Si 2p
Zn 3s
Zn 3p
O 2s
Zn 3d
Intensity (a. u.)
Binding Energy (eV)

(b)

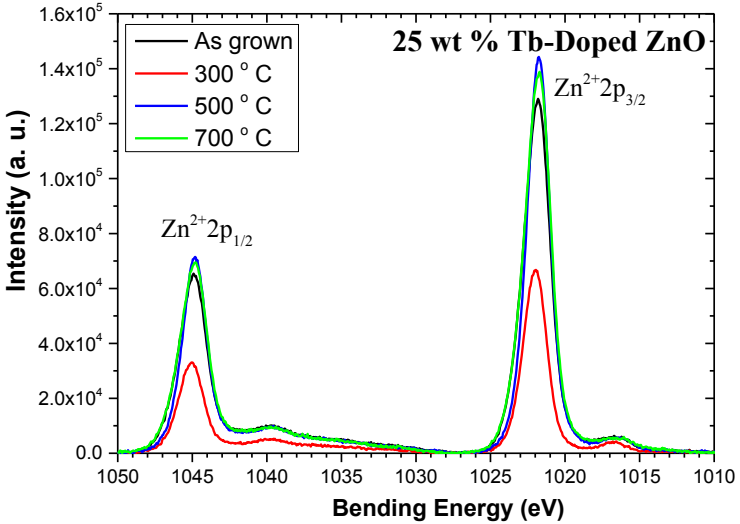
25 wt % Tb-Doped ZnO
As grown
300 ° C
500 ° C
700 ° C
$Zn^{2+}2p_{3/2}$
$Zn^{2+}2p_{1/2}$
Intensity (a. u.)
Bending Energy (eV)

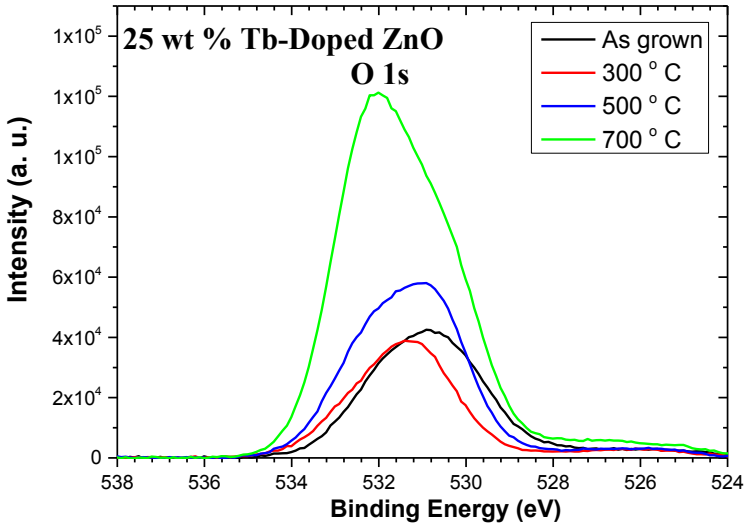
25 wt % Tb-Doped ZnO
O 1s
As grown
300 ° C
500 ° C
700 ° C
Intensity (a. u.)
Binding Energy (eV)

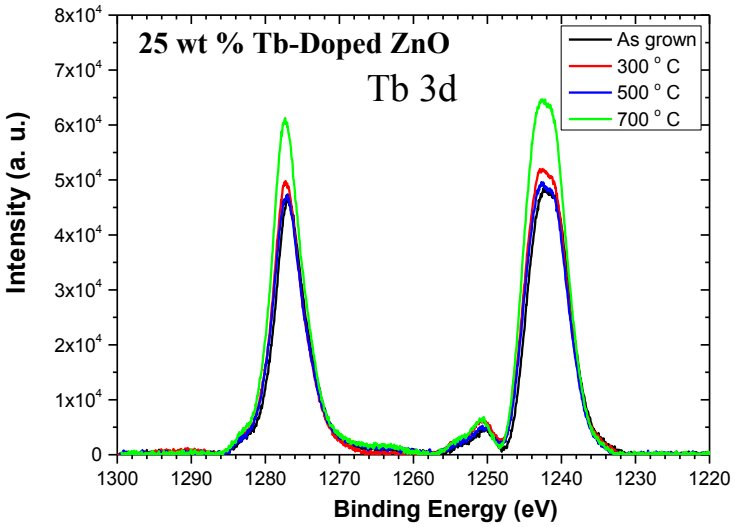
25 wt % Tb-Doped ZnO
Tb 3d
As grown
300 ° C
500 ° C
700 ° C
Intensity (a. u.)
Binding Energy (eV)

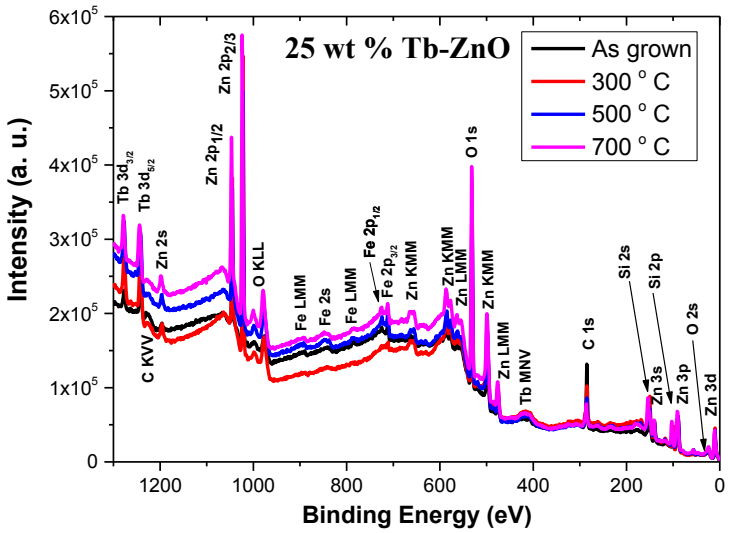
25 wt % Tb-ZnO
As grown
300 ° C
500 ° C
700 ° C
Tb $3d_{3/2}$
Tb $3d_{5/2}$
Zn 2s
Zn $2p_{3/2}$
Zn $2p_{1/2}$
O KLL
Fe LMM
Fe 2s
Fe LMM
Fe $2p_{1/2}$
Fe $2p_{3/2}$
Zn KMM
Zn LMM
Zn KMM
O 1s
Zn KMM
Zn LMM
Tb MNV
C 1s
Si 2s
Si 2p
Zn 3s
Zn 3p
O 2s
Zn 3d
C KVV
Intensity (a. u.)
Binding Energy (eV)

Figure 4

(a)

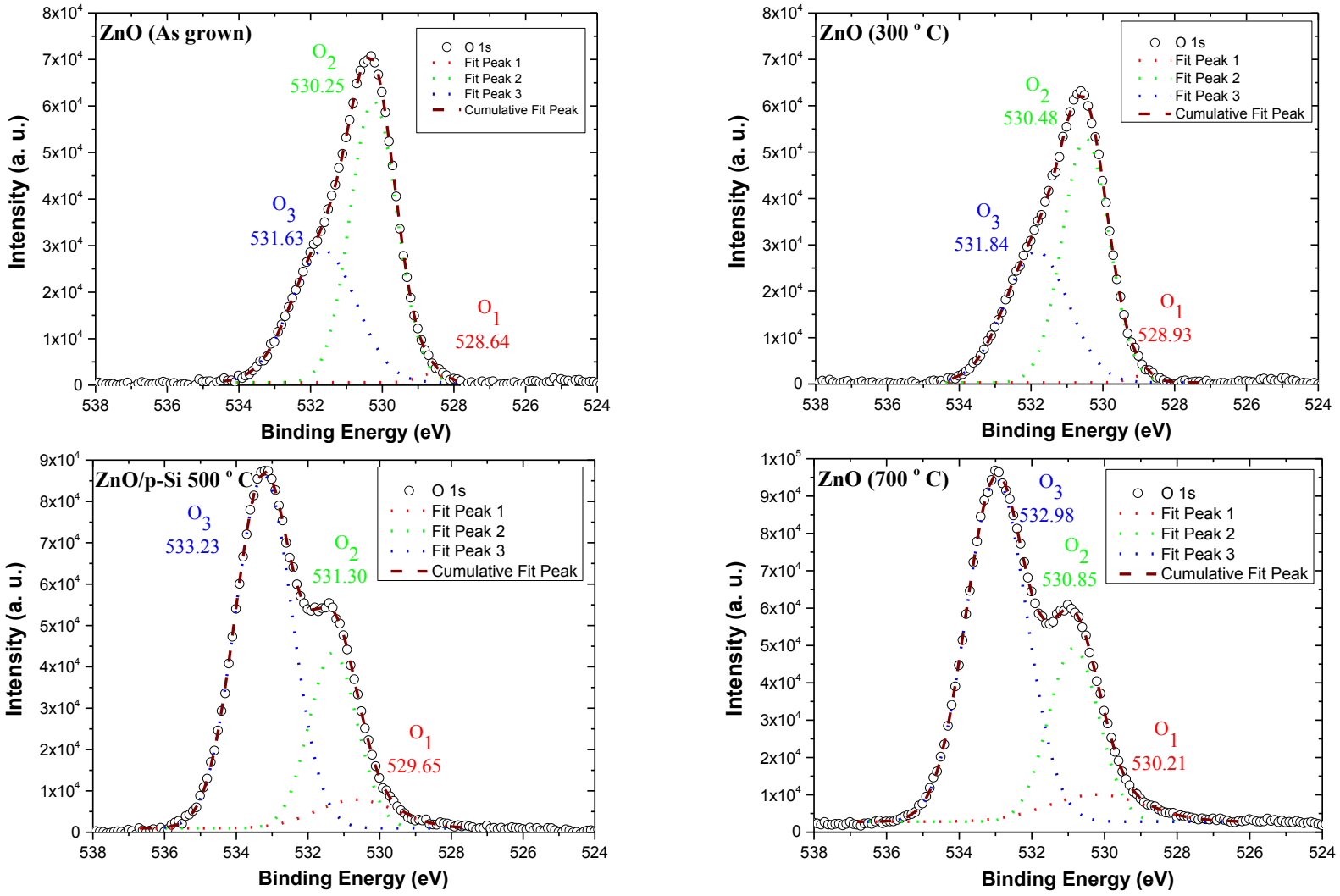
ZnO (As grown)
O 1s
Fit Peak 1
Fit Peak 2
Fit Peak 3
Cumulative Fit Peak
O2
530.25
O3
531.63
O1
528.64
Intensity (a. u.)
Binding Energy (eV)
ZnO (300 ° C)
O2
530.48
O3
531.84
O1
528.93
ZnO/p-Si 500 ° C
O3
533.23
O2
531.30
O1
529.65
ZnO (700 ° C)
O3
532.98
O2
530.85
O1
530.21

(b)

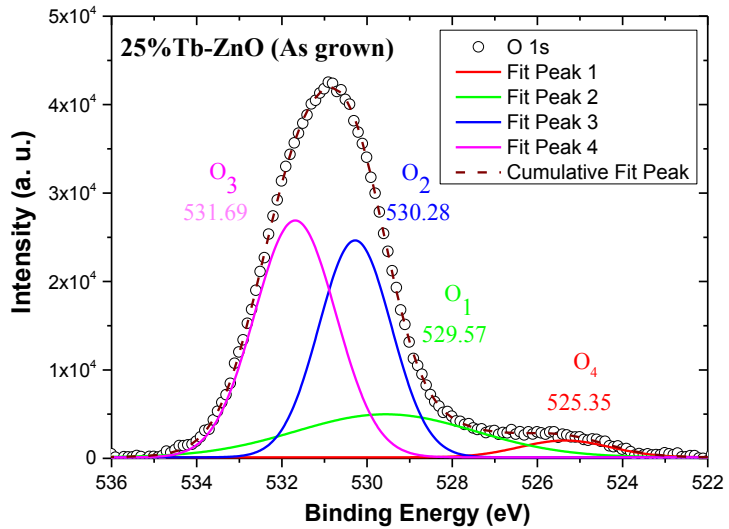
25%Tb-ZnO (As grown)
O 1s
Fit Peak 1
Fit Peak 2
Fit Peak 3
Fit Peak 4
Cumulative Fit Peak
O3
531.69
O2
530.28
O1
529.57
O4
525.35
Intensity (a. u.)
Binding Energy (eV)

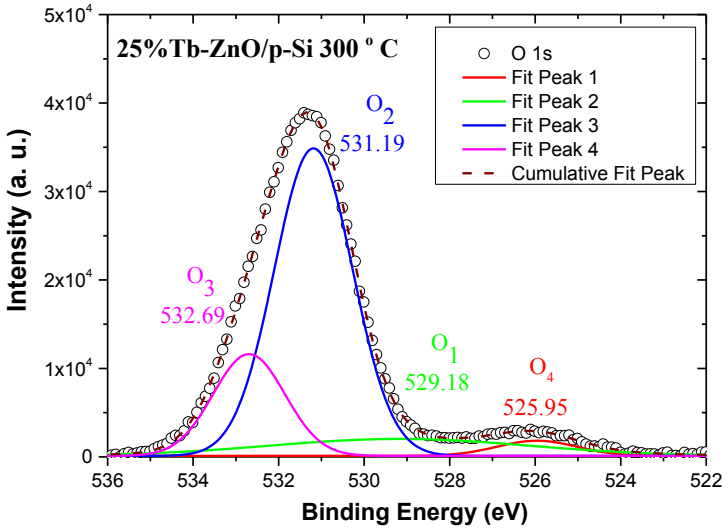
25%Tb-ZnO/p-Si 300 ° C
O 1s
Fit Peak 1
Fit Peak 2
Fit Peak 3
Fit Peak 4
Cumulative Fit Peak
O2
531.19
O3
532.69
O1
529.18
O4
525.95
Intensity (a. u.)
Binding Energy (eV)

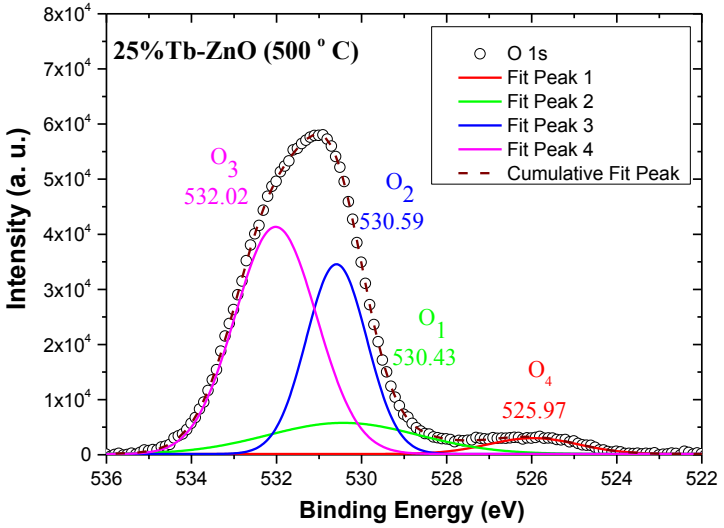
25%Tb-ZnO (500 ° C)
O 1s
Fit Peak 1
Fit Peak 2
Fit Peak 3
Fit Peak 4
Cumulative Fit Peak
O3
532.02
O2
530.59
O1
530.43
O4
525.97
Intensity (a. u.)
Binding Energy (eV)

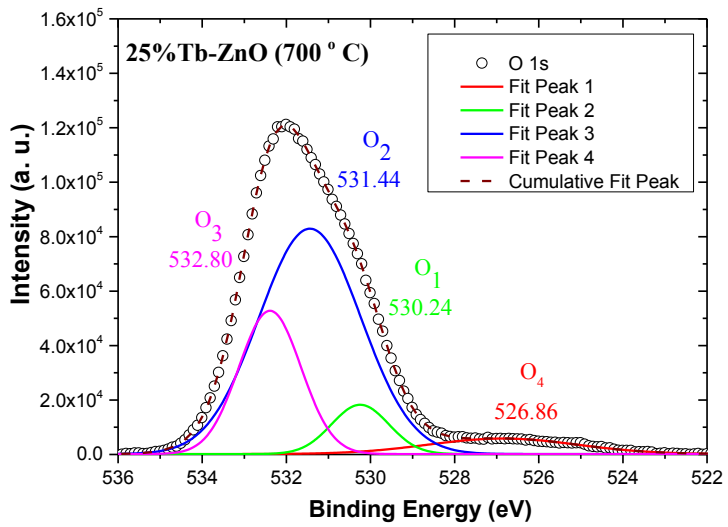
25%Tb-ZnO (700 ° C)
O 1s
Fit Peak 1
Fit Peak 2
Fit Peak 3
Fit Peak 4
Cumulative Fit Peak
O2
531.44
O3
532.80
O1
530.24
O4
526.86
Intensity (a. u.)
Binding Energy (eV)

Figure 5

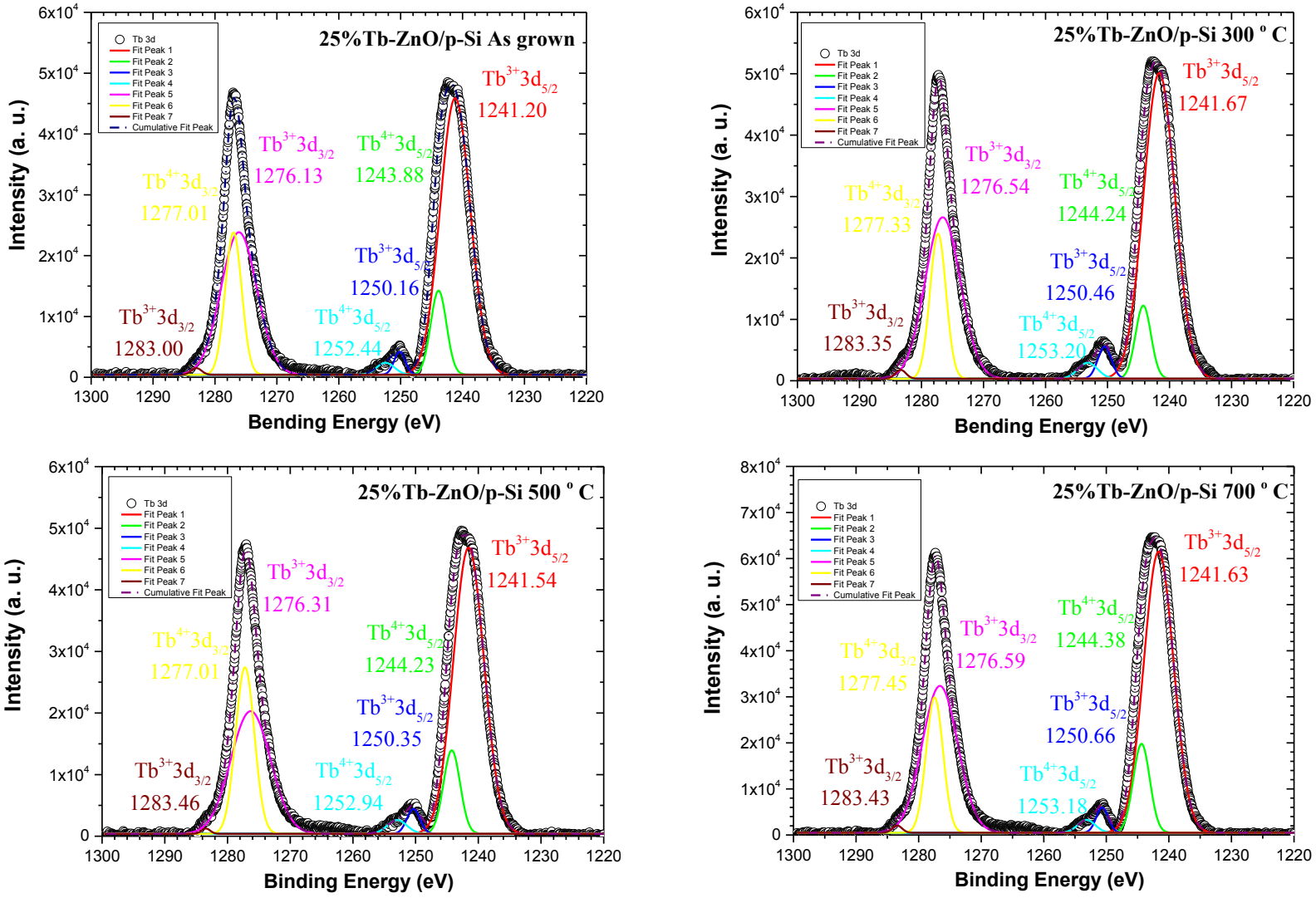
25%Tb-ZnO/p-Si As grown
Tb 3d
Fit Peak 1
Fit Peak 2
Fit Peak 3
Fit Peak 4
Fit Peak 5
Fit Peak 6
Fit Peak 7
Cumulative Fit Peak
Tb3+3d3/2 1276.13
Tb4+3d3/2 1277.01
Tb4+3d5/2 1243.88
Tb3+3d5/2 1241.20
Tb3+3d5/2 1250.16
Tb4+3d5/2 1252.44
Tb3+3d3/2 1283.00
Intensity (a. u.)
Bending Energy (eV)
25%Tb-ZnO/p-Si 300 ° C
Tb3+3d3/2 1276.54
Tb4+3d3/2 1277.33
Tb4+3d5/2 1244.24
Tb3+3d5/2 1241.67
Tb3+3d5/2 1250.46
Tb4+3d5/2 1253.20
Tb3+3d3/2 1283.35
Intensity (a. u.)
Bending Energy (eV)
25%Tb-ZnO/p-Si 500 ° C
Tb3+3d3/2 1276.31
Tb4+3d3/2 1277.01
Tb4+3d5/2 1244.23
Tb3+3d5/2 1241.54
Tb3+3d5/2 1250.35
Tb4+3d5/2 1252.94
Tb3+3d3/2 1283.46
Intensity (a. u.)
Binding Energy (eV)
25%Tb-ZnO/p-Si 700 ° C
Tb3+3d3/2 1276.59
Tb4+3d3/2 1277.45
Tb4+3d5/2 1244.38
Tb3+3d5/2 1241.63
Tb3+3d5/2 1250.66
Tb4+3d5/2 1253.18
Tb3+3d3/2 1283.43
Intensity (a. u.)
Binding Energy (eV)

Figure 6

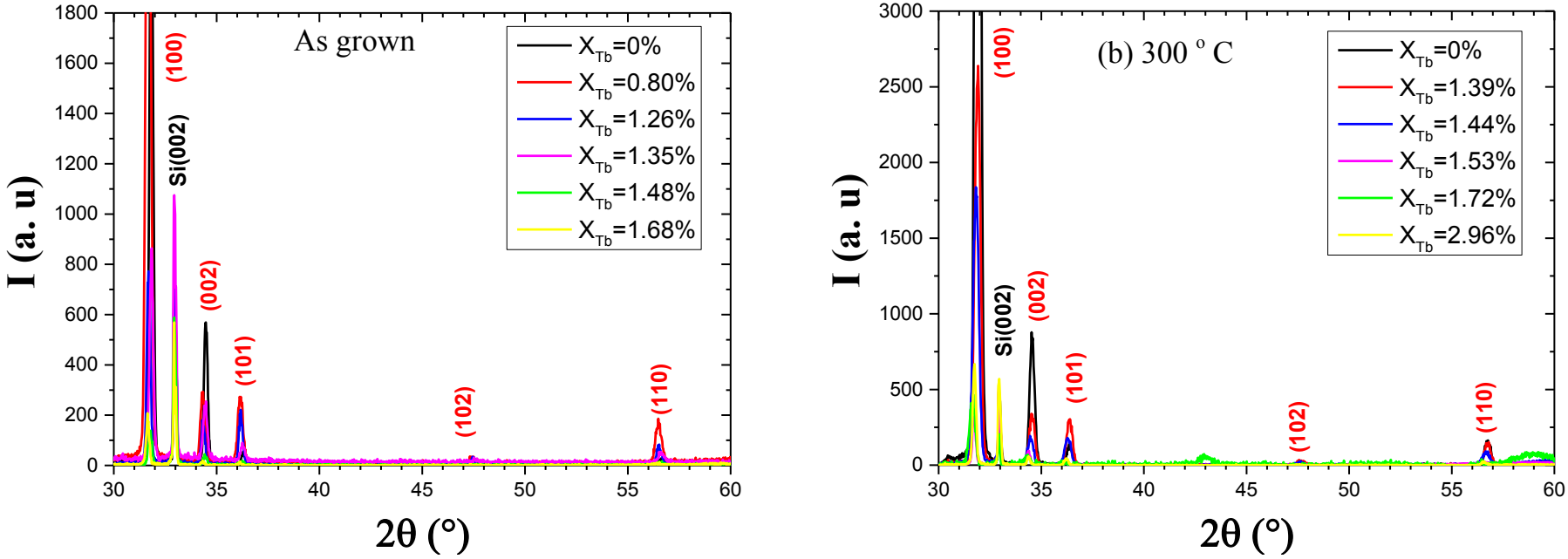
As grown
(b) 300 ° C
I (a. u)
2θ (°)
(100)
Si(002)
(002)
(101)
(102)
(110)
X_Tb=0%
X_Tb=0.80%
X_Tb=1.26%
X_Tb=1.35%
X_Tb=1.48%
X_Tb=1.68%
X_Tb=1.39%
X_Tb=1.44%
X_Tb=1.53%
X_Tb=1.72%
X_Tb=2.96%

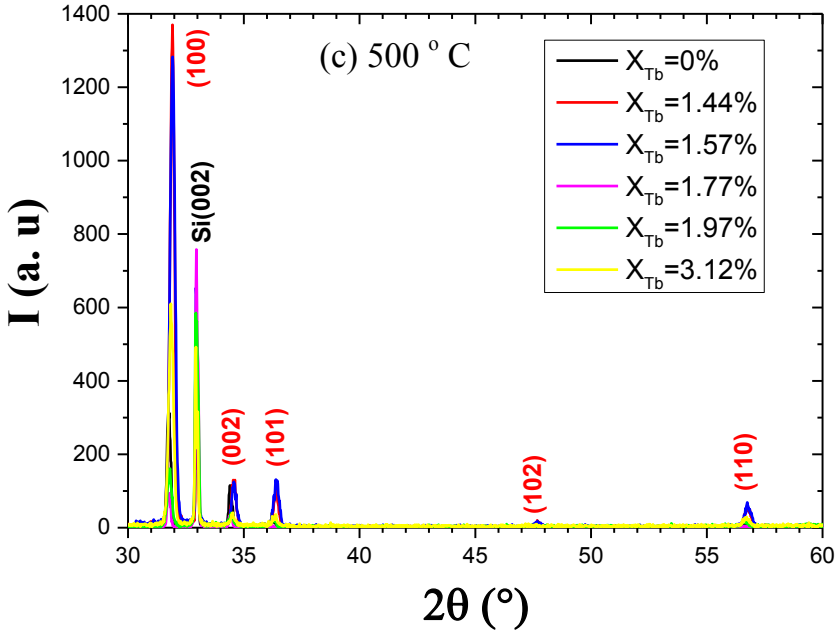
(c) 500 ° C
I (a. u)
2θ (°)
(100)
Si(002)
(002)
(101)
(102)
(110)
X_Tb=0%
X_Tb=1.44%
X_Tb=1.57%
X_Tb=1.77%
X_Tb=1.97%
X_Tb=3.12%

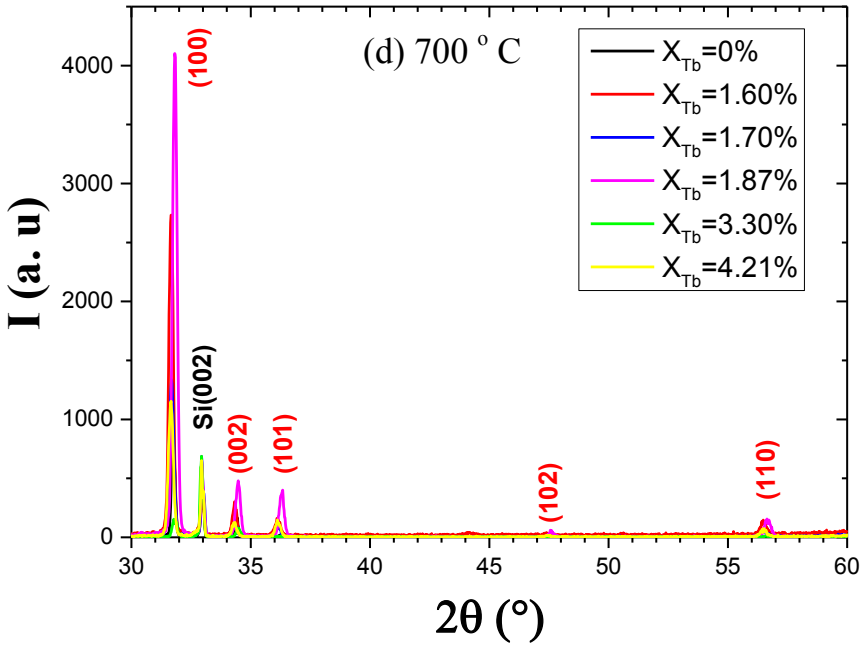
(d) 700 ° C
I (a. u)
2θ (°)
(100)
Si(002)
(002)
(101)
(102)
(110)
X_Tb=0%
X_Tb=1.60%
X_Tb=1.70%
X_Tb=1.87%
X_Tb=3.30%
X_Tb=4.21%

Figure 7

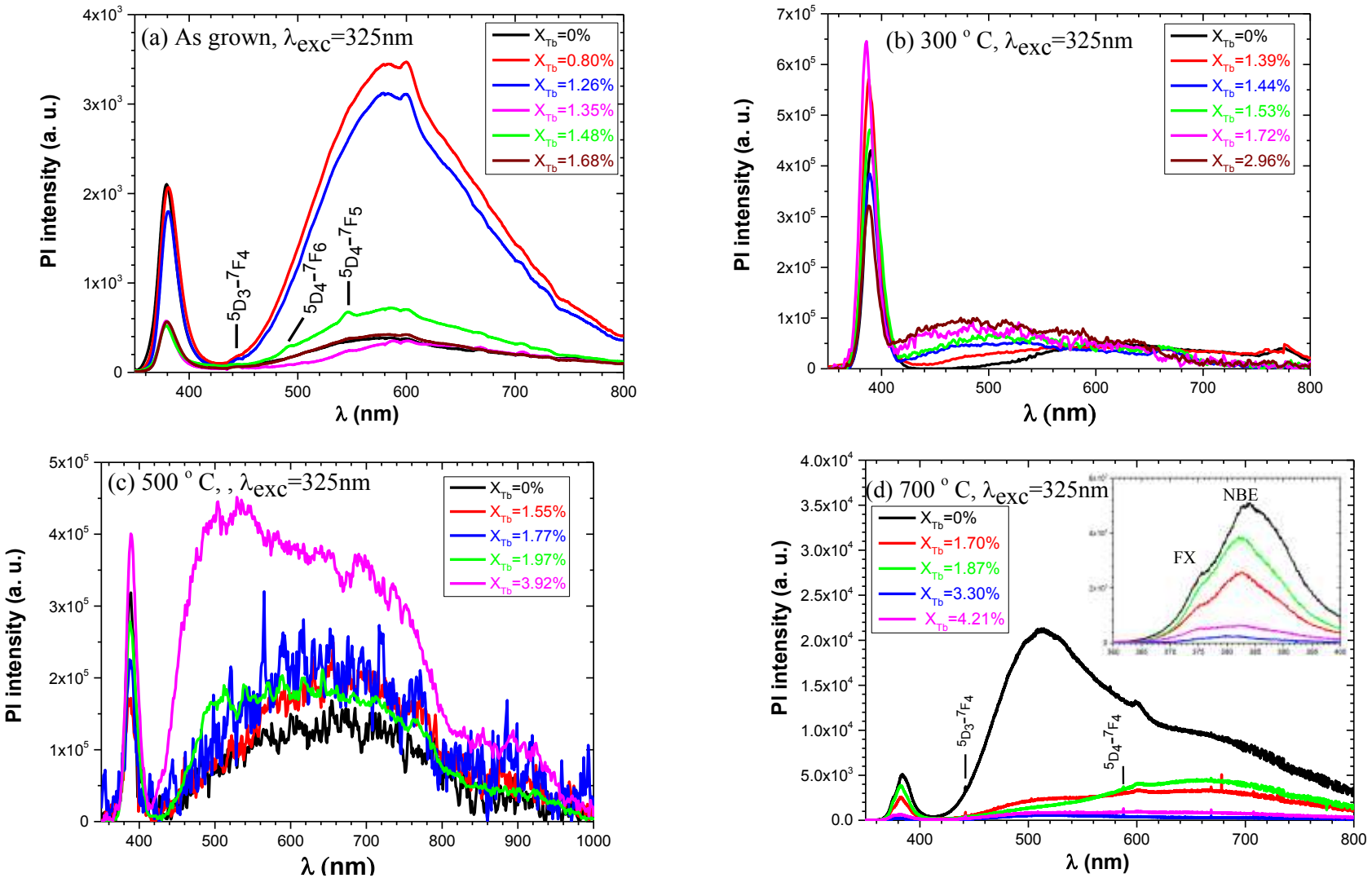
(a) As grown, λexc=325nm
XTb=0%
XTb=0.80%
XTb=1.26%
XTb=1.35%
XTb=1.48%
XTb=1.68%
5D3-7F4
5D4-7F6
5D4-7F5
PI intensity (a. u.)
λ (nm)
(b) 300 ° C, λexc=325nm
XTb=0%
XTb=1.39%
XTb=1.44%
XTb=1.53%
XTb=1.72%
XTb=2.96%
PI intensity (a. u.)
λ (nm)
(c) 500 ° C, , λexc=325nm
XTb=0%
XTb=1.55%
XTb=1.77%
XTb=1.97%
XTb=3.92%
PI intensity (a. u.)
λ (nm)
(d) 700 ° C, λexc=325nm
XTb=0%
XTb=1.70%
XTb=1.87%
XTb=3.30%
XTb=4.21%
NBE
FX
5D3-7F4
5D4-7F4
PI intensity (a. u.)
λ (nm)

Figure 8

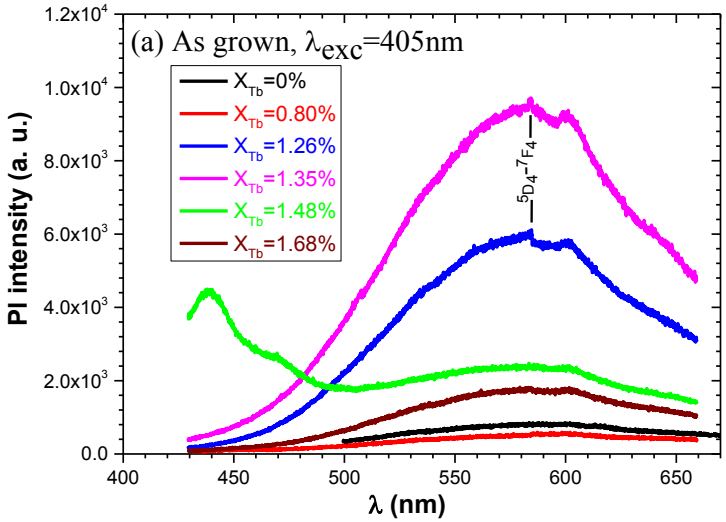
(a) As grown, λexc=405nm
XTb=0%
XTb=0.80%
XTb=1.26%
XTb=1.35%
XTb=1.48%
XTb=1.68%
5D4-7F4
PI intensity (a. u.)
λ (nm)
1.2x10^4
1.0x10^4
8.0x10^3
6.0x10^3
4.0x10^3
2.0x10^3
0.0
400
450
500
550
600
650

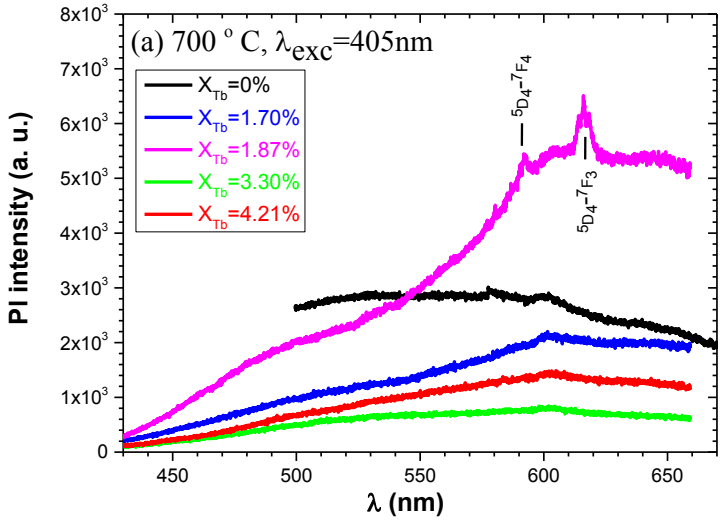
(a) 700 ° C, λexc=405nm
XTb=0%
XTb=1.70%
XTb=1.87%
XTb=3.30%
XTb=4.21%
5D4-7F4
5D4-7F3
PI intensity (a. u.)
λ (nm)
8x10^3
7x10^3
6x10^3
5x10^3
4x10^3
3x10^3
2x10^3
1x10^3
0
450
500
550
600
650

Figure 9

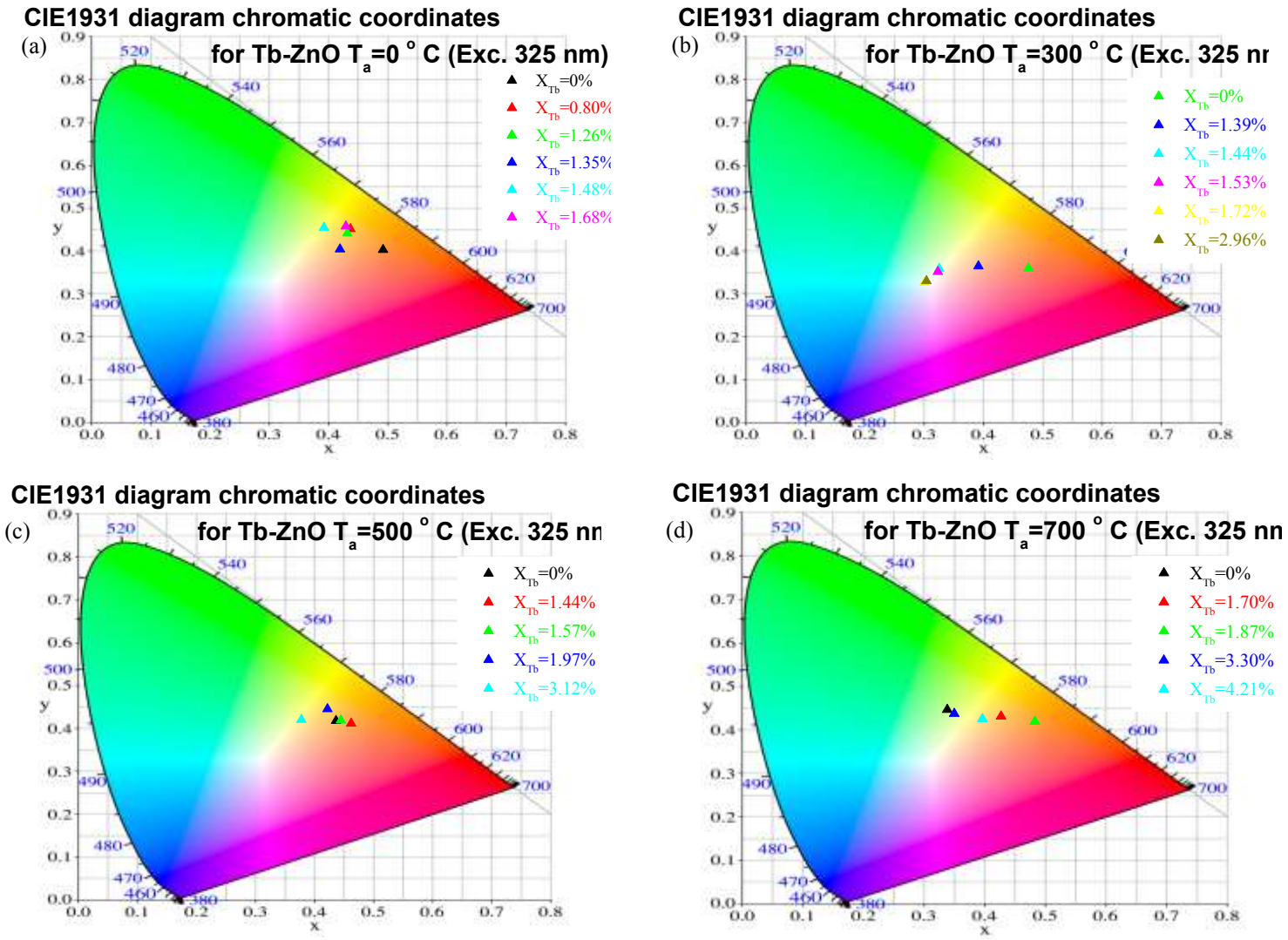
CIE1931 diagram chromatic coordinates
(a)
for Tb-ZnO T_a=0 ° C (Exc. 325 nm)
X_Tb=0%
X_Tb=0.80%
X_Tb=1.26%
X_Tb=1.35%
X_Tb=1.48%
X_Tb=1.68%
CIE1931 diagram chromatic coordinates
(b)
for Tb-ZnO T_a=300 ° C (Exc. 325 nr
X_Tb=0%
X_Tb=1.39%
X_Tb=1.44%
X_Tb=1.53%
X_Tb=1.72%
X_Tb=2.96%
CIE1931 diagram chromatic coordinates
(c)
for Tb-ZnO T_a=500 ° C (Exc. 325 nn
X_Tb=0%
X_Tb=1.44%
X_Tb=1.57%
X_Tb=1.97%
X_Tb=3.12%
CIE1931 diagram chromatic coordinates
(d)
for Tb-ZnO T_a=700 ° C (Exc. 325 nn
X_Tb=0%
X_Tb=1.70%
X_Tb=1.87%
X_Tb=3.30%
X_Tb=4.21%

Figure 10

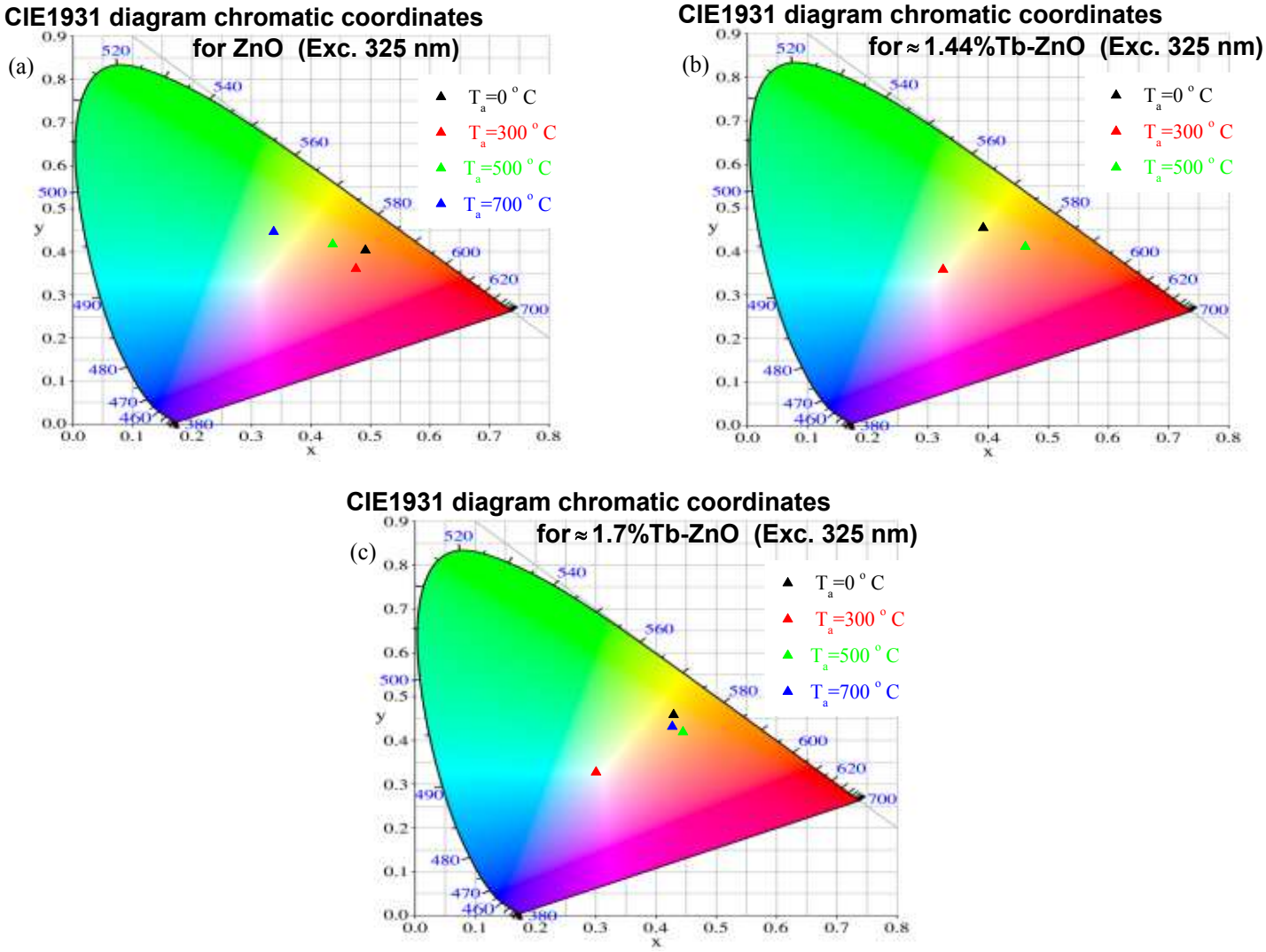
CIE1931 diagram chromatic coordinates
for ZnO (Exc. 325 nm)
(a)
T_a=0 ° C
T_a=300 ° C
T_a=500 ° C
T_a=700 ° C
CIE1931 diagram chromatic coordinates
for ≈ 1.44%Tb-ZnO (Exc. 325 nm)
(b)
T_a=0 ° C
T_a=300 ° C
T_a=500 ° C
CIE1931 diagram chromatic coordinates
for ≈ 1.7%Tb-ZnO (Exc. 325 nm)
(c)
T_a=0 ° C
T_a=300 ° C
T_a=500 ° C
T_a=700 ° C
x
y

Figure 11

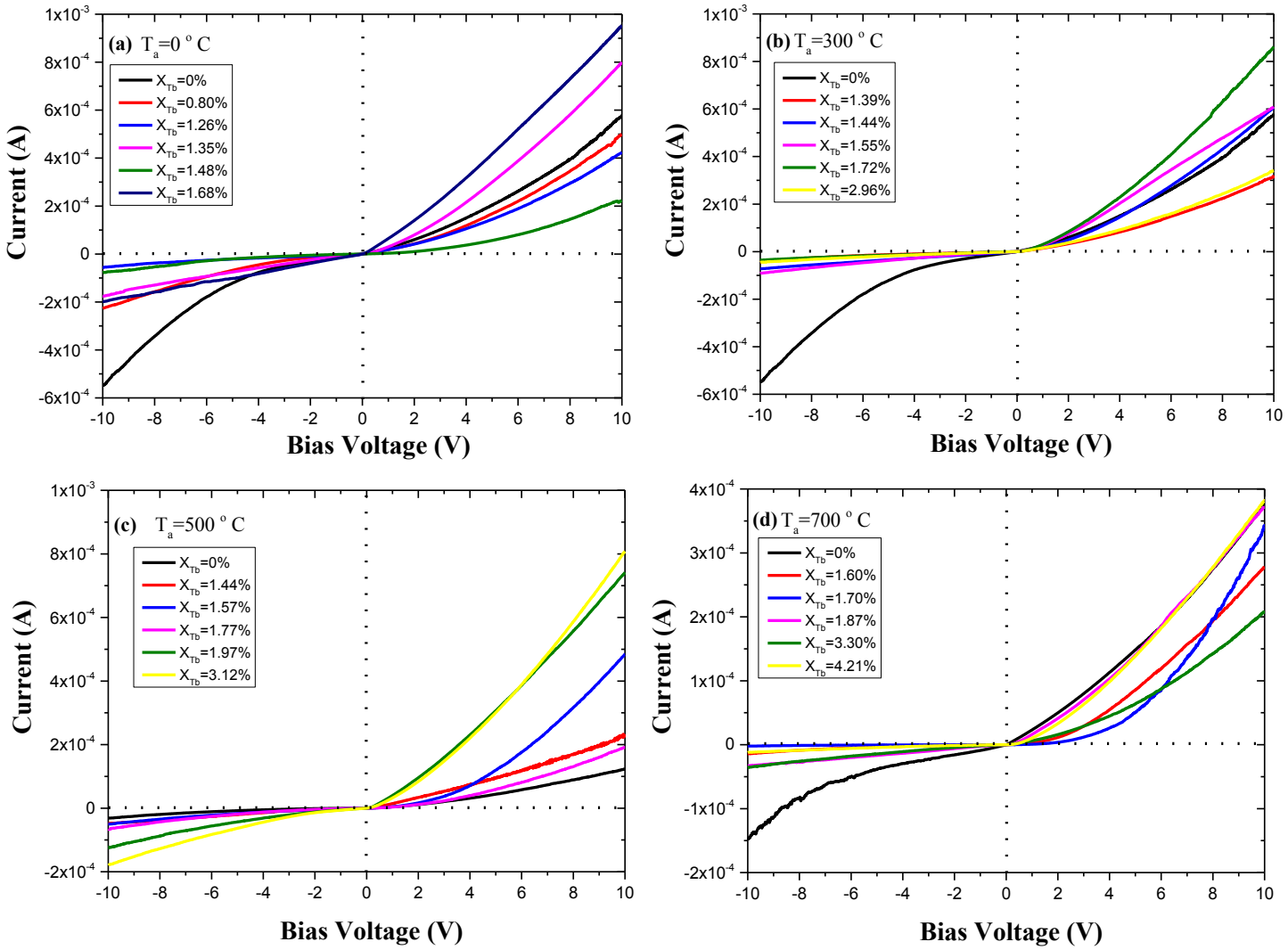
(a) T_a=0 ° C
X_Tb=0%
X_Tb=0.80%
X_Tb=1.26%
X_Tb=1.35%
X_Tb=1.48%
X_Tb=1.68%
(b) T_a=300 ° C
X_Tb=0%
X_Tb=1.39%
X_Tb=1.44%
X_Tb=1.55%
X_Tb=1.72%
X_Tb=2.96%
(c) T_a=500 ° C
X_Tb=0%
X_Tb=1.44%
X_Tb=1.57%
X_Tb=1.77%
X_Tb=1.97%
X_Tb=3.12%
(d) T_a=700 ° C
X_Tb=0%
X_Tb=1.60%
X_Tb=1.70%
X_Tb=1.87%
X_Tb=3.30%
X_Tb=4.21%
Current (A)
Bias Voltage (V)

Figure 12

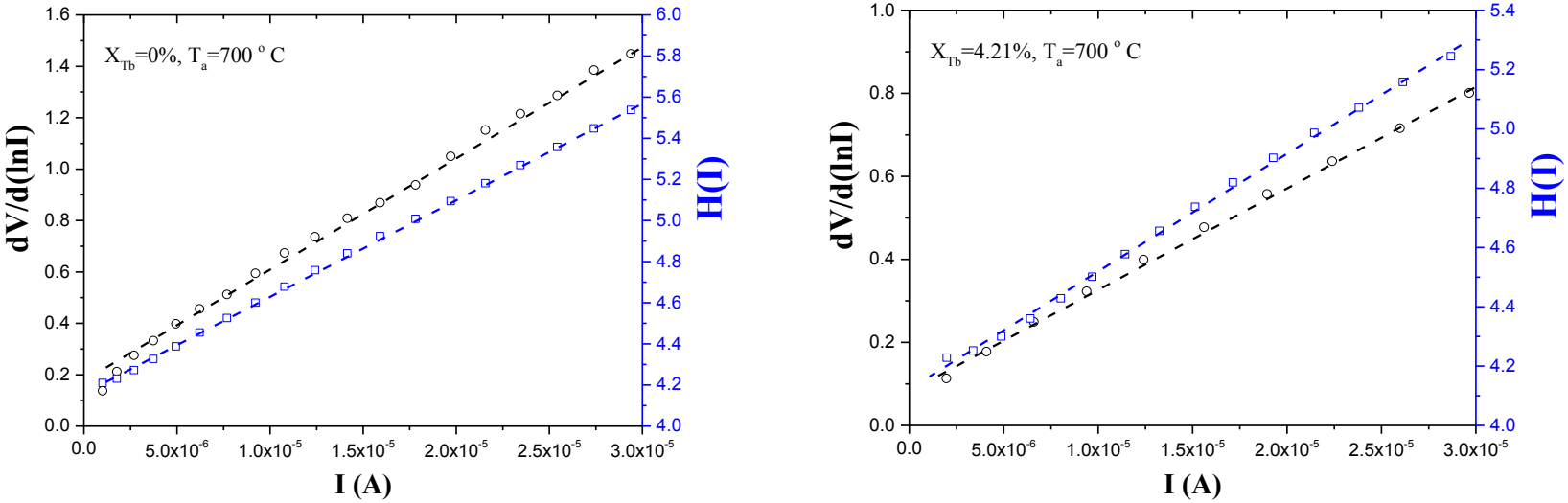

Table 1

Samples	T_a (°C)	X_{Tb}(%)
5%Tb-ZnO	0	0.80
	300	1.39
	500	1.44
	700	1.60
10%Tb-ZnO	0	1.26
	300	1.44
	500	1.57
	700	1.70
15%Tb-ZnO	0	1.35
	300	1.53
	500	1.77
	700	1.87
20%Tb-ZnO	0	1.48
	300	1.72
	500	1.97
	700	3.30
25%Tb-ZnO	0	1.68
	300	2.96
	500	3.12
	700	4.21

Table 2

Samples	T_a (° C)	O1s components	Peak position (eV)	Area ratio (%)
ZnO	0	O_1	528.64	1.44
		O_2	530.25	58.99
		O_3	531.63	39.57
	300	O_1	528.93	1.33
		O_2	530.48	56.29
		O_3	531.84	42.38
	500	O_1	528.65	8.90
		O_2	531.30	27.57
		O_3	533.23	63.53
	700	O_1	530.21	13.01
		O_2	530.85	26.68
		O_3	532.98	60.31
25%Eu-ZnO	0	O_1	529.57	4.47
		O_2	530.28	61.53
		O_3	531.69	34.00
	300	O_1	529.18	33.27
		O_2	531.19	36.52
		O_3	532.69	30.21
	500	O_1	530. 43	72.29
		O_2	530.59	12.54
		O_3	532.02	15.17
	700	O_1	530.24	32.55
		O_2	531.44	27.19
		O_3	532.80	40.26

Table 3

	Peak 1	**Peak 2**	**Peak 3**	**Peak 4**	**Peak 5**	**Peak 6**	**Peak 7**	**Peak 8**
T_a (°C)	$Tb3d_{5/2}$ (3+) (eV)	$Tb3d_{5/2}$ (4+) (eV)	$Tb3d_{5/2}$ (3+) (eV)	$Tb3d_{5/2}$ (4+) (eV)	$Tb3d_{3/2}$ (3+) (eV)	$Tb3d_{3/2}$ (4+) (eV)	$Tb3d_{3/2}$ (3+) (eV)	$Tb3d_{3/2}$ (4+) (eV)
0	1241.20	1243.88	1250.16	1252.44	1276.13	1277.01	1283.00	
300	1241.67	1244.24	1250.46	1253.20	1276.57	1277.33	1283.35	
500	1241.54	1244.23	1250.35	1252.94	1276.31	1277.01	1283.46	
700	1241.63	1244.38	1250.66	1253.18	1276.59	1277.45	1283.43	
Tb_2O_3 [28]	1241.2				1275.0			
$TbO_{1.5}$ (3+) [28]	1239.1		1250.4		1274.0		1286.3	
$TbO_{1.82}$ (4+) [28]		1241.4		1251.4		1276.0		1287.7

Table 4

T_a (°C)	XPS Area Zn 2p	XPS Area Tb^{3+} 3d	XPS Area Tb^{4+} 2p	C_{Tb}^{3+} (at %)	C_{Tb}^{4+} (at %)
0	434300	281670	47173	19.3	3.3
300	320274	202820	40224	18.8	3.7
500	396377	290549	47823	21.2	3.5
700	467692	370622	67991	22.3	4.1

Table 5

T_a (°C)	X_{Tb}(%)	t_{DS}(002) (nm)	δ_{DS}(200) (10^{14} lines/m^2)	t_{DS}(110) (nm)	δ_{DS}(110) (10^{14} lines/m^2)
0	0	41	5.95	28	12.78
	0.80	41	5.95	36	7.72
	1.26	40	6.25	34	8.65
	1.35	38	6.93	29	11.89
	1.48	38	6.93	34	8.65
	1.68	47	4.53	36	7.72
300	0	31	10.41	26	14.79
	1.39	27	13.72	27	13.72
	1.44	26	14.79	24	17.36
	1.53	40	6.25	29	11.89
	1.72	25	16.00	18	30.86
	2.96	44	5.17	35	8.16
500	0	52	3.73	74	1.83
	1.44	38	6.93	31	10.41
	1.57	37	7.30	30	11.11
	1.77	50	4.00	-	-
	1.97	37	7.30	32	9.77
	3.12	37	7.30	29	11.89
700	0	58	2,97	36	7.72
	1.60	42	5.67	32	9.77
	1.70	38	6.93	28	12.76
	1.87	38	6.93	30	11.11
	3.30	34	8.65	26	14.79
	4.21	35	8.16	25	16.00
ZnO powder	0	30	11.44	33	9.33

Table 6

T_a (°C)	X_{Tb}(%)	a (Å)	c (Å)	c/a	V (Å ^{3})	u	b (Å)	b_1(Å)
0	0	3.246	5.199	1.602	47.440	0.3799	1.9751	1.9754
	0.80	3.254	5.214	1.602	47.812	0.3798	1.9803	1.9805
	1.26	3.256	5.218	1.603	47.908	0.3798	1.9818	1.9817
	1.35	3.242	5.203	1.605	47.360	0.3794	1.9740	1.9741
	1.48	3.251	5.205	1.601	47.415	0.3800	1.9779	1.9782
	1.68	3.261	5.222	1.601	48.092	0.3800	1.9844	1.9843
300	0	3.240	5.187	1.601	47.156	0.3801	1.9716	1.9713
	1.39	3.239	5.188	1.602	47.136	0.3799	1.9709	1.9711
	1.44	3.245	5.199	1.602	47.411	0.3799	1.9751	1.9748
	1.53	3.253	5.201	1.603	47.783	0.3798	1.9772	1.9794
	1.72	3.261	5.223	1.602	48.101	0.3799	1.9842	1.9845
	2.96	3.252	5.212	1.603	47.735	0.3798	1.9795	1.9793
500	0	3.250	5.206	1.602	47.621	0.3799	1.9778	1.9778
	1.44	3.238	5.185	1.601	47.080	0.3800	1.9703	1.9703
	1.57	3.238	5.184	1.601	47.071	0.3800	1.9699	1.9702
	1.77	3.250	5.206	1.602	47.621	0.3799	1.9778	1.9778
	1.97	3.238	5.184	1.601	47.071	0.3800	1.9699	1.9873
	3.12	3.243	5.193	1.601	47.298	0.3800	1.9733	1.9733
700	0	3.251	5.209	1.602	47.678	0.3798	1.9784	1.9786
	1.60	3.258	5.220	1. 602	47.985	0.3799	1.9831	1.9827
	1.70	3.256	5.220	1.603	47.926	0.3797	1.9820	1.9820
	1.87	3.244	5.196	1.602	47.355	0.3799	1.9740	1.9742
	3.30	3.246	5,197	1.601	47.422	0.3800	1.9749	1.9752
	4.21	3.258	5.223	1.603	48.012	0.3797	1.9832	1.9832
ZnO powder	0	3.2502	5.2072	1.6021	47.639	0.3799	1.9780	1.9779
ZnO JCPDS (N◦ 36–1451)	0	3.2498	5.2066	1.6021	47.849	0.3799	1.9780	1.9777

Table 7

T_a (°C)	X_{Tb}(%)	E_g (eV)	
		Reflectance spectra	Pl spectra
0	0	3.20	3.27
	0.80	3.21	3.25
	1.26	3.22	3.26
	1.35	3.17	3.27
	1.48	3.18	3.27
	1.68	3.22	3.27
300	0	3.19	3.18
	1.39	3.24	3.19
	1.44	3.24	3.19
	1.53	3.19	3.19
	1.72	3.18	3.22
	2.96	3.20	3.19
500	0	3.21	3.20
	1.57	3.23	3.19
	1.77	3.20	3.19
	1.97	3.19	3.20
	3.12	3.17	3.19
700	0	3.20	3.23
	1.70	3.22	3.24
	1.87	3.23	3.24
	3.30	3.17	3.25
	4.21	3.21	3.24

Table 8

T_a (°C)	X_{Tb}(%)	CIE		CCT (K)
		x	*y*	
0	0	0.492	0.408	2300
	0.80	0.437	0.456	3395
	1.26	0.432	0.446	3415
	1.35	0.419	0.409	3381
	1.48	0.392	0.459	4199
	1.68	0.429	0.463	3557
300	0	0.476	0.365	2125
	1.39	0.392	0.370	3680
	1.44	0.326	0.364	5793
	1.53	0.323	0.357	5905
	1.72	0.301	0.331	7198
	2.96	0.304	0.335	6955
500	0	0.437	0.422	3172
	1.57	0.445	0.423	2734
	1.77	0.422	0.450	3046
	1.97	0.378	0.425	3598
	3.12	0.437	0.422	4348
700C	0	0.338	0.451	5378
	1.70	0.427	0.436	3427
	1.87	0.483	0.424	2529
	3.30	0.350	0.442	5076
	4.21	0.397	0.429	3970

Table 9

T_a (°C)	X_{Tb} (%)	I_F/I_R at ±4 V	Standard I-V method					Cheung - Cheung's method		
			V_F (V)	I_s (10^{-8} A)	n	φ_b (eV)	R_s (kΩ)	n	φ_b (eV)	R_s (kΩ)
0	0	1.98	3.36	7.15	1.51	0.82	11.7	2.63	0.73	31.8/33.1
	0.80	2.62	3.46	3.98	1.29	0.77	15.8	3.33	0.74	42.1/42.6
	1.26	6.27	1.88	2.34	1.92	0.83	10.6	5.80	0.73	25.6/26.0
	1.35	3.77	2.56	4.77	1.17	0.82	9.3	3.29	0.77	23.6/20.2
	1.48	2.67	2.44	4.77	1.44	0.85	57.8	5.60	0.76	111.8/119.2
	1.68	3.88	1.09	10.3	1.16	0.82	9.2	3.33	0.73	11.7/12.1
300	0	1.95	2.48	9.54	1.36	0.81	15.5	3.14	0.76	34.4/35.4
	1.39	8.56	2.84	0.795	1.71	0.87	23.1	2.24	0.78	54.8/54.3
	1.44	5.33	2.68	10.73	1.24	0.81	11.8	4.24	0.74	38.0/37.0
	1.53	7.29	1.07	4.77	1.24	0.90	34.0	2.60	0.78	26.7/24.5
	1.72	19.24	2.34	2.39	1.28	0.85	17.9	2.70	0. 74	37.7/38.3
	2.96	6.64	2.95	2.38	1.31	0.85	21.3	2.24	0.79	48.1/51.7
500	0	6.22	2.27	1.19	3.33	0.87	63.8	4.33	0.77	86.7/89.7
	1.44	5.26	1.67	3.97	1.25	0.84	36.2	1.20	0.83	66.2/58.0
	1.57	5.77	4.00	3.58	1.51	0.84	12.2	5.00	0.79	51.1/49.9
	1.77	3.20	3.40	0.29	1.67	0.90	34.0	5.70	0.83	91.8/103.3
	1.97	7.40	1.69	5.96	1.26	0.83	10.9	2.71	0.77	17.3/17.9

	3.12	5.02	2.53	5.92	1.00	0.83	9.3	2.90	0.80	21.2/19.0
700	0	3.86	0.69	9.54	1.27	0.83	44.4	5.40	0.77	45.9/47.4
	1.60	2.23	3.27	1.19	1.62	0.87	24.6	3.36	0.78	105.3/109.7
	1.70	88.78	5.32	0.79	3.87	0.88	14.0	5.37	0.87	59.9/64.5
	1.87	7.70	1.99	0.80	1.51	0.88	20.7	7.23	0.88	25.3/29.2
	3.30	4.19	3.69	3.58	1.11	0.84	31.1	6.07	0.85	91.7/84.9
	4.21	30.50	2.33	1.19	2.67	0.87	19.4	4.72	0.83	35.8/41.6